JGR Planets

RESEARCH ARTICLE
10.1029/2022JE007291

Key Points:

- We develop a formulation to calculate the secular acceleration of Phobos due to tidal dissipation in Mars
- Using the Love number k_2 and the secular acceleration s, we obtain for Mars a core size of 1,820 ± 80 km and a bulk Q of 93.0 ± 8.40
- We discuss several means to distinguish between Mars models using seismological, rotational, and lithospheric observations

Supporting Information:

Supporting Information may be found in the online version of this article.

Correspondence to:

L. Pou,
lpou@ucsc.edu

Citation:

Pou, L., Nimmo, F., Rivoldini, A., Khan, A., Bagheri, A., Gray, T., et al. (2022). Tidal constraints on the Martian interior. *Journal of Geophysical Research: Planets*, *127*, e2022JE007291. https://doi.org/10.1029/2022JE007291

Received 9 MAR 2022
Accepted 26 SEP 2022

Author Contributions:

Conceptualization: L. Pou, F. Nimmo
Formal analysis: L. Pou, F. Nimmo, A. Rivoldini, A. Khan, A. Bagheri, T. Gray, H. Samuel, P. Lognonné, A.-C. Plesa, T. Gudkova
Funding acquisition: F. Nimmo
Investigation: L. Pou, A. Rivoldini
Methodology: L. Pou, F. Nimmo, A. Rivoldini, A. Khan, P. Lognonné, A.-C. Plesa
Project Administration: F. Nimmo
Software: L. Pou, F. Nimmo, A. Rivoldini, A. Khan
Supervision: L. Pou, F. Nimmo, D. Giardini
Validation: L. Pou, F. Nimmo, A. Rivoldini, A. Khan, A. Bagheri, T. Gray, H. Samuel, P. Lognonné, A.-C. Plesa, T. Gudkova
Visualization: L. Pou, F. Nimmo
Writing – original draft: L. Pou

Tidal Constraints on the Martian Interior

L. Pou[1], F. Nimmo[1], A. Rivoldini[2], A. Khan[3,4], A. Bagheri[3], T. Gray[3], H. Samuel[5], P. Lognonné[5], A.-C. Plesa[6], T. Gudkova[7], and D. Giardini[3]

[1]Department of Earth and Planetary Sciences, University of California Santa Cruz, Santa Cruz, CA, USA, [2]Royal Observatory of Belgium, Brussels, Belgium, [3]Institute of Geophysics, ETH Zürich, Zürich, Switzerland, [4]Physik-Institut, University of Zurich, Zurich, Switzerland, [5]Institut de Physique du Globe de Paris, CNRS, Université Paris Cité, Paris, France, [6]Institute of Planetary Research, German Aerospace Center (DLR), Berlin, Germany, [7]Schmidt Institute of Physics of the Earth, Russian Academy of Sciences, Moscow, Russia

Abstract We compare several recent Martian interior models and evaluate how these are impacted by the tidal constraints provided by the Love number k_2 and the secular acceleration in longitude s of its main moon, Phobos. The expression of the latter is developed up to harmonic degree 5 to match the accuracy of the current observations. We match a number of current interior structure models to the recent measurements of the tidal parameters and derive estimations of the possible core radius, temperature profile, and attenuation in the Martian interior. Our estimation of the core radius is 1,820 ± 80 km, consistent with recent seismic measurements. The attenuation profiles in the Martian interior at the main tidal period of Phobos are similar between the considered models, giving a range for the degree-2 bulk tidal attenuation $Q_2 = 93.0 \pm 8.40$ but diverge at seismic frequencies. At seismic frequencies, model shear attenuation Q_μ ranges between 100 and 4,000 in the lower mantle, so that a measurement of seismic shear attenuation could be used as an effective means for distinguishing between the models considered. Other constraints such as elastic lithosphere thickness and Chandler Wobble period favor a thicker elastic lithosphere and models with a frequency dependence α of the shear attenuation between 0.15 and 0.4. Improved constraints on the Martian interior should be possible with additional seismic and radio observations from the InSight mission.

Plain Language Summary The largest moon of Mars, Phobos, raises tides on the red planet causing its surface to be deformed. The size of this tidal bulge depends on the elastic properties of Mars, while viscosity and anelasticity inside the planet cause the tidal bulge to be misaligned with the position of Phobos on its orbit. This misalignment between Phobos and the tidal bulge of Mars creates an acceleration in longitude for the moon, which can be measured and used with the size of the tidal bulge to constraint the interior of Mars. Both the size and orientation of the tidal bulge can be used as tidal constraints to probe the size of the core of Mars, the temperature profile in its interior, and how strong the viscous dissipation is in its mantle. Our current estimates give a wide range of possible attenuation in the Martian mantle, favoring larger core sizes with larger elastic thickness of the lithosphere, the rigid outermost layer of a solid planet. Knowledge of the Martian interior could be further improved with future seismic and radio measurements from the InSight mission.

1. Introduction

The study of the tidal response of Mars provides insights into the interior properties of the planet, and especially its deep structure (e.g., Lognonné & Mosser, 1993; Van Hoolst et al., 2003). The value of the second degree tidal Love number measured from orbit implies the presence of a liquid core (Yoder et al., 2003) and can be used to constrain the density and size of the core, including the mantle rigidity, when combined with other measurements such as moment of inertia or bulk density. The secular acceleration s of Phobos has been measured to high precision from both ground-based observations and observations of Phobos' shadow on Mars by Mars Express and direct observations of Phobos by the Mars Reconnaissance Orbiter (e.g., Bills et al., 2005; Jacobson, 2010). Because of its proximity to Mars, the orbital evolution of Phobos is of particular interest as it is driven by the tidal dissipation occurring inside the Martian mantle, which, among other parameters, depends on its temperature structure and rheology (Bagheri et al., 2019, 2021; Khan et al., 2018; Nimmo & Faul, 2013). This dissipation is often quantified by the tidal quality factor Q, where a large Q value means small dissipation.

Because of the proximity of Phobos to Mars, higher degree tides are required to fully describe the tidal response of Mars (Bills et al., 2005). While only the degree-2 Love number has been measured, the measurement of the

Writing – review & editing: L. Pou, F. Nimmo, A. Rivoldini, A. Khan, A. Bagheri, T. Gray, H. Samuel, P. Lognonné, A.-C. Plesa, T. Gudkova, D. Giardini

secular acceleration of Phobos has reached a level of accuracy that is sensitive to higher degrees. With increasing tidal degree, the depth probed by tides becomes shallower, allowing for additional constraints to be put on the shallower parts of the Martian interior. Hence, both the secular acceleration and the tidal Love number can be used to improve our knowledge of the Martian interior. One important complication is that periods of the solar tide (24.6 hr) and each of the tides raised by Phobos for degrees 2–5 (between 2.2 and 11.1 hr) are different; as a result, any attempt to model these effects must specify how tidal dissipation varies with frequency.

In this work, we will examine how several different models of the Martian interior (to be described in the following section) make use of the Love number and the secular acceleration of Phobos to constrain characteristics of Mars such as mantle temperature and core size. By matching existing models with the most recent values of the Love number and the secular acceleration and comparing the different models, we can gain insight into which features are model-independent, and thus likely to be more robust. We proceed by first expanding the Martian tidal potential up to degree 5 and applying it to derive an expression for the secular acceleration of Phobos. By fitting or matching the measured Love number and secular acceleration for each model, we get a range of possible core sizes and temperature profiles for the Martian interior and compute their respective shear attenuation Q_μ profiles at the tidal frequencies of Phobos. We then discuss several means of distinguishing between the constructed models by relying on elastic lithospheric thickness, seismic measurements, and Chandler wobble period.

2. Previous Works

Various interior models of Mars have been proposed based on numerous observations of the red planet, including compositional estimates from Martian meteorites and in situ observations (e.g., G. J. Taylor, 2013; Wänke & Dreibus, 1994), gravity and topography measurements (e.g., Genova et al., 2016; Wieczorek & Zuber, 2004), thermal evolution (Plesa et al., 2018; Samuel et al., 2019), and geophysical modeling from laboratory experiments (e.g., Zharkov & Gudkova, 1997; Zharkov et al., 2017). The inferred tidal response of Mars, mainly through the second degree Love number of Mars at the solar tide k_2^s, has also been used to derive the density and rigidity structure of Mars (e.g., Khan & Connolly, 2008; Nimmo & Faul, 2013; Rivoldini et al., 2011; Yoder et al., 2003; Zharkov & Gudkova, 2005). However, many of these studies did not focus on the tidal dissipation factor Q which provides pertinent information on the thermal structure of the Martian mantle and that can be constrained by measuring of the secular acceleration of Phobos (e.g., Bagheri et al., 2019; Khan et al., 2018; Nimmo & Faul, 2013).

To explain the observed bulk dissipation Q value, several different attenuation models have been proposed. Castillo-Rogez and Banerdt (2012) derived a mantle temperature around 1700 K using an Andrade rheology based on dry olivine. Nimmo and Faul (2013) used an approach with a modified Burgers model based on the laboratory experiments of Jackson and Faul (2010). With an assumed grain size of 1 cm and fitting the bulk density, moment of inertia, and tidal Love number of Mars, they estimated a present-day mantle potential temperature of 1625 ± 75 K but did not consider a detailed multimineral structure model of the Martian mantle as their focus was not on rigidity but attenuation.

Using a set of interior structure models based on the Wänke-Dreibus mineralogy (Wänke & Dreibus, 1994), Zharkov et al. (2017) constructed a shear attenuation profile for the silicate shell of Mars assuming the Earth's profile for Mars based on the similarity between Earth's geotherm and the commonly employed areotherms for Mars (e.g., Plesa et al., 2016; Verhoeven et al., 2005; Zharkov et al., 2009). This approach used a simplified piecewise attenuation profile with a relatively low frequency exponent that describes the frequency dependence of Q to match the secular acceleration of Phobos in contrast to more recent works (e.g., Bagheri et al., 2019; Khan et al., 2018).

Samuel et al. (2019) modeled the thermochemical history of a Mars-like planet coupled to the orbital evolution of Phobos to constrain the rheology of the Martian mantle and the initial state of the planet. They combined the constraint that Phobos remained below the synchronous orbit during at least the last four Gyr of its evolution with the requirement that Mars' core produced a magnetic field early in Mars' history, together with constraints on the cooling of the Martian mantle during the Amazonian-Hesperian periods (Baratoux et al., 2011) and with the requirement that Mars' mantle remained in convective state until the present-day, as suggested by the recent traces of volcanism at the surface of Mars (Hartmann et al., 1999; Neukum et al., 2004). However, while their

expression for the secular acceleration accounted for tides up to degree 4, they fixed the Love number ratios k_2/k_3 and k_2/k_4 rather than explicitly calculating higher degree terms, and Phobos remaining below the synchronous orbit for so long was shown to be unlikely in Bagheri et al. (2021).

Khan et al. (2018) and Bagheri et al. (2019) used laboratory-based viscoelastic dissipation models to construct geophysically constrained models of Mars. They used a parametric approach where mantle seismic properties are computed using Gibbs free energy minimization (Connolly, 2009) to compute stable mantle mineralogy and seismic properties as a function of pressure, temperature, and period based on the thermodynamic formulations and parameters of Stixrude and Lithgow-Bertelloni (2005) and Stixrude and Lithgow-Bertelloni (2011). Based on this parameterization, they inverted the degree-2 Love number, mean mass, global dissipation, and moment of inertia of Mars but not higher degrees terms that enters the expression for the secular acceleration.

Based on the detection of the Chandler Wobble of Mars, Konopliv et al. (2020) constructed interior structure models of Mars using a frequency dependent dissipation model to explain the observed period of the Chandler wobble, diurnal solar tide, and secular acceleration of Phobos (up to degree 5). Although, Konopliv et al. (2020) show that the dissipation model used can well describe all those observations, it is less suited to infer knowledge about the local temperature structure of the mantle since it is based on a depth-independent description. Like previous works, they did not highlight how the specifics of the orbital parameters of Phobos (low eccentricity, inclination, and equatorial location for the tidal bulge of Mars) impact the derivation of the full secular acceleration expression.

3. Tidal Constraints of Mars

3.1. Observations

As Phobos orbits Mars, the moon causes a gravitational pull on the planet which responds to this external forcing by deforming. The amount of deformation of Mars depends on its internal structure and on the tidal potential of Phobos, which can be expressed as a sum of Legendre polynomials (Kaula, 1964):

$$V(r) = \frac{Gm^*}{d} \sum_{\ell=2}^{\infty} \left(\frac{r}{d}\right)^{\ell} P_{\ell}(\cos S), \tag{1}$$

where G is the gravitational constant, m^* is the mass of Phobos, d is the distance between Phobos and the center of Mars, and P_{ℓ} is the Legendre polynomial of degree ℓ. r is the distance between the center of Mars and the point where the tidal potential V is calculated, and S is the solid angle between the axis linking the center of Mars to the aforementioned point and the sub-Phobos point on the Martian surface. Because of the $\frac{r}{d}$ term, the tidal potential is usually restricted to degree 2. For the solar tides on Mars, the value of $\frac{r}{d}$ is around 10^{-5}; however, for the Phobos tides on Mars this term is roughly equal to 0.36 (Jacobson & Lainey, 2014; Seidelmann et al., 2007). Given the large contribution of the $\frac{r}{d}$ term, higher degree tides need to be considered (Bills et al., 2005).

The tidal forcing from Phobos distorts the shape of Mars and creates displacements, changes in gravitational potential, and variations of surface gravity. These are quantified by the Love numbers h, k, and l (Love, 1911; Shida, 1912), which depend on the internal structure and rheology of the planet and are frequency-dependent (e.g., Efroimsky & Lainey, 2007). Changes in the gravitational potential can be measured by tracking the position of an orbiter. The most recent determination of the Love number k_2^s of Mars for the degree-2 solar tide based on Mars Odyssey, Mars Reconnaissance Orbiter, and Mars Global Surveyor observations is given in Table 1. Because Love numbers are frequency-dependent, it is important to keep track of their related tidal degree, order, and forcing origin. In the remainder of this paper, Love numbers related to the solar tides are annotated with an s exponent, while Phobos-tide related Love numbers are designated by degree ℓ, order m, and eccentricity and inclination indexes p and q (see Section 3.2) such as k_{2200} for instance.

If Mars was purely elastic, the tidal bulge of Mars would be perfectly aligned with the position of Phobos along its orbit. However, anelastic dissipation occurring in the Martian interior causes the tidal bulge to be misaligned by an angle called the lunitidal interval (Redmond & Fish, 1964) or geometric lag angle (MacDonald, 1964). This is expressed as a phase lag ϵ to be added to the solid angle S in Equation 1 (Kaula, 1964). This angle depends on the internal structure of Mars and more particularly on internal dissipation, characterized by a frequency-dependent

Table 1
Reference Table for the Physical and Orbital Parameters of the Mars-Phobos System

Tidal parameter	Value	Article source
Main solar tide Love number k_2^s	0.174 ± 0.008	Konopliv et al. (2020)
Phobos secular acceleration s	1.273 ± 0.003 mdeg.yr^{-2}	Jacobson and Lainey (2014)
Mass of Phobos m*	$1.0596 \pm 0.0019\ 10^{16}$ kg	Pätzold et al. (2014)
Phobos semi-major axis a*	9,376 km	Seidelmann et al. (2007)
Phobos eccentricity e*	0.0151	Seidelmann et al. (2007)
Phobos inclination i*	0.046°	Seidelmann et al. (2007)
Phobos mean motion n	1128.8 deg.day^{-1}	Jacobson and Lainey (2014)
Mass of Mars m	$6.4172\ 10^{23}$ kg	Konopliv et al. (2011)
Mean radius of Mars r	3389.5 km	Seidelmann et al. (2007)
Period of Chandler Wobble P_{CW}	206.9 ± 0.5 days	Konopliv et al. (2020)

Note. This work focuses on the second degree tidal Love number k_2^s value for the main solar tide on Mars and Phobos secular acceleration s. Parameters uncertainties are given when they are not negligible for our fits and calculations.

quality factor Q (e.g., Efroimsky & Lainey, 2007; Efroimsky & Makarov, 2013; Murray & Dermott, 2000; P. A. Taylor & Margot, 2010). Since Phobos' orbit lies below the areostationary orbit, the misaligned tidal bulge of Mars lags behind the position of Phobos and creates a braking effect on it, causing a deceleration in longitude on the Martian satellite. Observations of Phobos using ground-based telescopes, imaging from spacecraft, and spacecraft tracking during flybys can be combined to determine the ephemerides of Phobos to great accuracy from which its secular acceleration s can be obtained. The value of Phobos' secular acceleration value used here is given in Table 1.

To be able to accurately fit our models to the secular acceleration of Phobos, we need to expand the relation between the secular acceleration, the geometric lag angle, and the tidal potential of Mars and its quality factor to an accuracy of the order of magnitude of the error bars given in Table 1. The greatest harmonic degree ℓ of the tides considered will be used to match the aforementioned error bars.

3.2. Derivation of the Secular Acceleration of Phobos

Typically, tidal response models only consider degree-2 tides and assume that higher degrees can be neglected. Given the measured secular acceleration of Phobos and the Love number k_2^s, this assumption allows derivation of the tidal bulk Q_2 of Mars (Jacobson, 2010; Jacobson & Lainey, 2014). However, in the case of Phobos and Mars, the contribution of higher degree terms cannot be neglected due to the proximity of the two planetary bodies. Here, we develop the expression for the secular acceleration of Phobos by taking higher degree terms into account.

The expression for the tidal potential of Mars given by Equation 1 can be expanded in terms of colatitude and longitude of the Martian point (θ, ϕ) where the potential is calculated and in terms of Keplerian elements of Phobos' orbit with inclination i*, eccentricity e*, argument of the periapsis ω*, argument of the ascending node Ω*, and mean anomaly M* (Kaula, 1964):

$$V = \frac{Gm^*}{a^*} \sum_{\ell=2}^{\infty} \left(\frac{r}{a^*}\right)^{\ell} \sum_{\substack{m=0 \\ \ell-m \text{ even}}}^{\ell} \frac{(\ell-m)!}{(\ell+m)!} (2-\delta_{0m})\, P_{\ell m}(\cos\theta) \sum_{p,q} F_{\ell mp}(i^*)\, G_{lpq}(e^*) \left(\cos m\phi \begin{Bmatrix} \cos \\ \sin \end{Bmatrix}_{\substack{\ell-m \text{ odd} \\ \ell-m \text{ even}}} ((\ell-2p)\omega^* + (\ell-2p+q)M^* + m(\Omega^*)) + \sin m\phi \begin{Bmatrix} \sin \\ -\cos \end{Bmatrix}_{\ell-m \text{ odd}} ((\ell-2p)\omega^* + (\ell-2p+q)M^* + m(\Omega^*)) \right). \quad (2)$$

Here, a^* is the semimajor axis of Phobos, ℓ and m are the degree and order of the tide, respectively, and p and q are indexes related to the polynomial functions of the inclination and eccentricity of Phobos $F_{\ell mp}(i^*)$ and $G_{\ell pq}(e^*)$, respectively. Because of the small inclination ($i^* = 0.046°$) and eccentricity ($e^* = 0.0151$) of Phobos (Jacobson & Lainey, 2014), we will for now consider only the order 0 terms in inclination and eccentricity in Equation 2 for the polynomials $F_{\ell mp}$ and $G_{\ell pq}$. The neglected terms (orders 1 in e^* and i^*) impact the secular acceleration for around 0.1% of the order 0 terms related to eccentricity and around 0.001% of the order 0 terms related to inclination (Boué & Efroimsky, 2019).

For degree 2, only the terms $\ell mpq = 2200$ and $\ell mpq = 2010$ are nonzero at order 0 in terms of either inclination or eccentricity:

$$\begin{aligned} F_{\ell mp=220} &= 3 \\ G_{\ell pq=220} &= 1 \\ F_{\ell mp=201} &= -\frac{1}{2} \\ G_{\ell pq=210} &= 1 \end{aligned} \tag{3}$$

resulting in the following degree-2 tidal potential terms:

$$V_{2200} = \frac{3}{4}\frac{Gm^* r^2}{a^{*3}}\left(1-\cos^2\theta\right)\left[\cos\left(2\omega^* + 2M^* + 2\Omega^* - 2\phi\right)\right], \tag{4}$$

$$V_{2010} = -\frac{Gm^* r^2}{a^{*3}}\frac{1}{4}\left(3\cos^2\theta - 1\right). \tag{5}$$

Adding V_{2200} and V_{2010} yields the resultant degree-2 tidal potential:

$$\begin{aligned} V_2(r) &= V_{2200} + V_{2010} \\ &= \frac{Gm^*}{a^*}\left(\frac{r}{a^*}\right)^2\frac{1}{4}\left(3\left(1-\cos^2\theta\right)\cos\left(2\omega^* + 2M^* + 2\Omega^* - 2\phi\right) - 3\cos^2\theta + 1\right) \\ &= \frac{Gm^*}{a^*}\left(\frac{r}{a^*}\right)^2\frac{1}{4}\left(3\sin^2\theta\left[2\cos^2\left(\omega^* + M^* + \Omega^* - \phi\right) - 1\right] - 3\cos^2\theta + 1\right) \\ &= \frac{Gm^*}{a^*}\left(\frac{r}{a^*}\right)^2\frac{1}{4}\left(3\sin^2\theta 2\cos^2\left(\omega^* + M^* + \Omega^* - \phi\right) - 3 + 1\right) \\ &= \frac{Gm^*}{a^*}\left(\frac{r}{a^*}\right)^2\frac{1}{4}\left(3\left[2\sin^2\theta\cos^2\left(\omega^* + M^* + \Omega^* - \phi\right) - 1\right] + 1\right). \end{aligned} \tag{6}$$

Note here that in this general case, the second to last constant term -1 has contributions from both V_{2200} and V_{2010}, making the first term of the right side of the last line of Equation 6 a combination of these two potentials. We can rewrite Equation 6 in terms of the solid angle S between a point at the surface of Mars with colatitude and longitude (θ, ϕ) and the sub-Phobos point with longitude $(\omega^* + M^* + \Omega^*)$. Making use of the fact that $\cos S = \sin\theta\cos(\phi - \omega^* - M^* - \Omega^*)$, we have the following equation:

$$\begin{aligned} V_2(r) &= \frac{Gm^*}{a^*}\left(\frac{r}{a^*}\right)^2\frac{1}{4}\left(3\left(2\cos^2(S) - 1\right) + 1\right) \\ &= \frac{Gm^*}{a^*}\left(\frac{r}{a^*}\right)^2\frac{1}{4}\left(3\cos(2S) + 1\right) \\ &= \frac{Gm^*}{a^*}\left(\frac{r}{a^*}\right)^2 P_2\left(\cos S\right), \end{aligned} \tag{7}$$

which is the same as Equation 1 for degree $\ell = 2$ but with $d = a^*$, as expected since we neglected eccentricity. As mentioned before, the identification of the $\cos(2S)$ term with V_{2200} and the constant term $+1$ of Equation 7 with V_{2010} is only strictly true when the tidal potential is studied close to the equator, that is, for $\theta = 90°$. This is due to the fact that V_{2010} depends on the colatitude where the tidal potential is calculated as illustrated in Equation 5 and therefore can contribute to the $\cos(2S)$ term, especially in polar regions. Since we are neglecting the inclination of Phobos with Mars and are studying the tidal bulge of Mars raised by its largest moon, this identification is nevertheless possible.

The spatial distribution of the tidal forcing due to the different degrees can hence be expressed using the Legendre polynomial $P_\ell(\cos(S))$ of the corresponding degree ℓ, with S being the angular distance between the considered Martian location and the sub-Phobos point:

$$\begin{aligned} P_3(\cos(S)) &= \frac{1}{8}\left(5\cos(3S) + 3\cos(S)\right), \\ P_4(\cos(S)) &= \frac{1}{64}\left(35\cos(4S) + 20\cos(2S) + 9\right), \\ P_5(\cos(S)) &= \frac{1}{128}\left(63\cos(5S) + 35\cos(3S) + 30\cos(S)\right), \end{aligned} \tag{8}$$

corresponding to tides $\ell mpq = 3300, 3110, 4400, 4210, 4020, 5500, 5310$, and 5120 in accordance with the footnote 9 in P. A. Taylor and Margot (2010). The order m of the tide-raising potential corresponds to the argument of the cosine in the Legendre polynomial of degree ℓ and indicates the frequency dependence of the separate terms for a given degree. For order $m = 1$, the corresponding period is Phobos' synodic period $T_1 = 11$ hr 06 min, while higher orders periods are given by $T_m = T_1/m$.

The link between secular acceleration and the geometric lag angle or LTI (lunitidal interval) when neglecting eccentricity is (Bills et al., 2005; Redmond & Fish, 1964) as follows:

$$\frac{1}{n}\frac{dn}{dt} = -3\alpha_m n \sum_{\ell=2} k_{\ell mpq}\mathcal{F}_\ell(\gamma)\left(\frac{r}{a^*}\right)^{2\ell+1}, \tag{9}$$

where n is the mean motion, $k_{\ell mpq}$ are the Love numbers related to the potentials $V_{\ell mpq}$ seen before, γ is the geometric lag angle, and $\mathcal{F}_\ell$ and α_m are defined as follows:

$$\begin{aligned} \mathcal{F}_\ell(\gamma) &= \frac{dP_\ell(\gamma)}{d\gamma}, \\ \alpha_m &= \frac{m^*}{m}, \end{aligned} \tag{10}$$

where P_ℓ is the Legendre polynomial of degree ℓ and m^* and m are the mass of Phobos and Mars, respectively. By convention, the secular acceleration s is defined as (Bills et al., 2005; Jacobson & Lainey, 2014; Lainey et al., 2007) follows:

$$s = \frac{1}{2}\frac{dn}{dt}. \tag{11}$$

Using the identification of the different degrees and orders of the tides in the tidal potential mentioned in Equations 7 and 8, we can calculate the different values of $\mathcal{F}_\ell$ for $\ell = 2$ to $\ell = 5$:

$$\begin{aligned} \mathcal{F}_2(\gamma) &= -\frac{3}{2}\sin\left(2\gamma_{2200}\right), \\ \mathcal{F}_3(\gamma) &= -\frac{3}{8}\left(\sin\left(\gamma_{3110}\right) + 5\sin\left(3\gamma_{3300}\right)\right), \\ \mathcal{F}_4(\gamma) &= -\frac{5}{16}\left(2\sin\left(2\gamma_{4210}\right) + 7\sin\left(4\gamma_{4400}\right)\right), \\ \mathcal{F}_5(\gamma) &= -\frac{15}{128}\left(2\sin\left(\gamma_{5120}\right) + 7\sin\left(3\gamma_{5310}\right) + 21\sin\left(5\gamma_{5500}\right)\right), \end{aligned} \tag{12}$$

Note that no $m = 0$ terms appear as expected because they denote an axisymmetric gravity field component, which generates deformation not affected by any phase lag. We can relate the geometric lag angle γ of Redmond and Fish (1964) (also called geometric lag angle $\delta_{\ell mpq}$ in MacDonald [1964]) to the tidal quality factor $Q_{\ell mpq}$ ([P. A. Taylor & Margot, 2010]):

$$Q^{-1}_{\ell mpq} = m\delta_{\ell mpq} = m\gamma_{\ell mpq} \tag{13}$$

which is related to the phase lag $\epsilon_{\ell mpq}$ defined by Kaula (1964) for large Q values:

$$|\epsilon_{\ell mpq}| = \frac{1}{Q_{\ell mpq}} \tag{14}$$

The expression for the secular acceleration up to degree 5 thus becomes

$$\begin{aligned}\frac{1}{n}\frac{dn}{dt} = 3\alpha_m n \Bigg[& k_{2200}\frac{3}{2}\sin(2\gamma_{2200})\left(\frac{r}{a^*}\right)^5 \\ & + \frac{3}{8}\left(k_{3110}\sin(\gamma_{3110}) + 5k_{3300}\sin(3\gamma_{3300})\right)\left(\frac{r}{a^*}\right)^7 \\ & + \frac{5}{16}\left(2k_{4210}\sin(2\gamma_{4210}) + 7k_{4400}\sin(4\gamma_{4400})\right)\left(\frac{r}{a^*}\right)^9 \\ & + \frac{15}{128}\left(2k_{5120}\sin(\gamma_{5120}) + 7k_{5310}\sin(3\gamma_{5310}) + 21k_{5500}\sin(5\gamma_{5500})\right)\left(\frac{r}{a^*}\right)^{11}\Bigg],\end{aligned} \tag{15}$$

or if changing the geometric lag angle into Q factors:

$$\begin{aligned}\frac{1}{n}\frac{dn}{dt} = 3\alpha_m n \Bigg[& \frac{3}{2}\frac{k_{2200}}{Q_{2200}}\left(\frac{r}{a^*}\right)^5 \\ & + \frac{3}{8}\left(\frac{k_{3110}}{Q_{3110}} + 5\frac{k_{3300}}{Q_{3300}}\right)\left(\frac{r}{a^*}\right)^7 \\ & + \frac{5}{16}\left(2\frac{k_{4210}}{Q_{4210}} + 7\frac{k_{4400}}{Q_{4400}}\right)\left(\frac{r}{a^*}\right)^9 \\ & + \frac{15}{128}\left(2\frac{k_{5120}}{Q_{5120}} + 7\frac{k_{5310}}{Q_{5310}} + 21\frac{k_{5500}}{Q_{5500}}\right)\left(\frac{r}{a^*}\right)^{11}\Bigg].\end{aligned} \tag{16}$$

Compared to degree $\ell = 2$, the terms for degree $\ell = 5$ are smaller by a factor of $(r/a^*)^6$, which is approximately 0.2%. This is the order of magnitude of the error bar on the secular acceleration thus the inclusion of this term. While this is significantly higher than the inclination terms mentioned in Equation 2, this is also the order of magnitude of the larger eccentricity terms in Equation 2 and therefore they must be taken into account for $\ell = 2$. Details of the calculations for these terms are given in Appendix A. The secular acceleration thus becomes

$$\begin{aligned}\frac{1}{n}\frac{dn}{dt} = 3\alpha_m n \Bigg[& \left(\frac{3}{2}\frac{k_{2200}}{Q_{2200}} + e^{*2}\left(\frac{9}{8}\frac{k_{2011}}{Q_{2011}} + \frac{3}{16}\frac{k_{220-1}}{Q_{220-1}} + \frac{441}{16}\frac{k_{2201}}{Q_{2201}} - \frac{15}{2}\frac{k_{2200}}{Q_{2200}}\right)\right)\left(\frac{r}{a^*}\right)^5 \\ & + \frac{3}{8}\left(\frac{k_{3110}}{Q_{3110}} + 5\frac{k_{3300}}{Q_{3300}}\right)\left(\frac{r}{a^*}\right)^7 \\ & + \frac{5}{16}\left(2\frac{k_{4210}}{Q_{4210}} + 7\frac{k_{4400}}{Q_{4400}}\right)\left(\frac{r}{a^*}\right)^9 \\ & + \frac{15}{128}\left(2\frac{k_{5120}}{Q_{5120}} + 7\frac{k_{5310}}{Q_{5310}} + 21\frac{k_{5500}}{Q_{5500}}\right)\left(\frac{r}{a^*}\right)^{11}\Bigg].\end{aligned} \tag{17}$$

The periods at which the four eccentricity terms $k_{\ell mpq}$ and $Q_{\ell mpq}$ are calculated are no longer related to the synodic period T_1 of Phobos, making Equation 13 invalid. Instead, these terms must be calculated at the following periods (Efroimsky & Williams, 2009; Kaula, 1964):

$$T_{\ell mpq} = \frac{2\pi}{|(\ell - 2p + q)n - m\dot{\phi}|} \tag{18}$$

where $\dot{\phi}$ is the spin rate of Mars. This general expression of the period $T_{\ell mpq}$ is also valid for the potentials with neglected eccentricity, but as these potentials follow $\ell - 2p + q = m$, their respective periods relate directly to the synodic period (i.e., $n - \dot{\phi}$) of Phobos rather than the orbital period (with n) and the sidereal period of Mars (with $\dot{\phi}$) separately.

A common assumption in some previous works is to neglect the frequency dependence of the Love number k by using only the $k_{\ell\ell 00}$ values. However, as indicated in Equation 8, a single degree has contributions from multiple frequencies based on the order of the tides as displayed by the different coefficients in the cosine functions. Therefore, considering only a single frequency for computing the Love numbers can create an estimated difference in the final secular acceleration between 0.1% and 0.2% depending on the Martian model, which is of the order of magnitude of the error bars on the secular acceleration of Phobos. For comparison, the main solar tide k_2^s is between 0.5% and 1% larger than the main Phobos tide k_{2200} (also referred as k_{22} or k_2 in other works [e.g., Yoder et al., 2003]). Our derivation of the secular acceleration is consistent with the works of Renaud et al. (2021), Boué and Efroimsky (2019), and Bagheri et al. (2021); however, Renaud et al. (2021) and Boué

Table 2
Nominal Parameters for Models Used in This Work

Model name	Core radius (km)	Elastic lithospheric thickness (km)	CMB temperature (K)	Frequency dependence α	Love number k_{2200}
FN cold	1,790	125	1,694	0.3	0.167
FN hot	1,820	275	1,759	0.3	0.168
AB Andrade	1,800	270	1,880	0.32	0.168
AB Burgers	1,800	260	1,860	0.33	0.167
HS1	1,850	290	2,060	0.2	0.171
HS2	1,830	260	2,020	0.15	0.169
HS3	1,855	320	2,020	0.33	0.170
TG	1,828	244	2,075	0.1	0.168
AR - TA 85	1,770	262	2,095	0.3	0.170
AR - TA 111	1,770	333	2,175	0.3	0.170
AR - YO 85	1,780	262	2,095	0.3	0.168
AR - YO 111	1,760	333	2,175	0.3	0.169

Note. k_{2200} is the Love number for the main Phobos tide at 5.55 hr.

and Efroimsky (2019) truncated their calculations at degree 2, while Bagheri et al. (2021) truncated at degree 3.

Since Q is also frequency dependent, there are also several frequencies that should be considered for a given degree (Bagheri et al., 2019, 2021; Efroimsky & Lainey, 2007). Just like the various $k_{\ell mpq}$, the degree 5 Q_{5500} for instance should be calculated at $T_5 = 2$ hr 13 min, but Q_{5310} should be calculated at $T_3 = 3$ hr 42 min and Q_{5120} should be calculated at $T_1 = 11$ hr 06 min, that is, Phobos' synodic period. Taking only the main order for each tidal degree can decrease the resulting secular acceleration by several percent, exceeding the current error bars. In our calculations of the Love numbers and the secular acceleration, all $k_{\ell mpq}$ and $Q_{\ell mpq}$ are frequency-dependent according to the degrees ℓ and orders m indicated in the previous equations as the first indices ℓmpq of the tides considered.

The contribution of each degree to the secular acceleration of Phobos is mainly governed by the ratio $\frac{r}{a^*}$ of the Martian radius to the semimajor axis of Phobos. In terms of the orders of magnitude, this means that the contribution of degree 4 is about 0.34% of the total secular acceleration for ℓ from 2 to 4. Since the most recent relative error bars on the secular acceleration are closer to 0.24% (Table 1), degree 5 also needs to be taken into account. Its terms have a relative contribution of 0.02% to the final secular acceleration of Phobos.

The four degree-2 terms dependent on the eccentricity e^* are also frequency dependent and must be calculated at their respective period given by Equation 18. As such, the first term $\ell mpq = 2011$ must be calculated at $T_{2011} = 7$ hr 39 min, which is the orbital period of Phobos, while $T_{220-1} = 20$ hr 14 min, $T_{2201} = 3$ hr 13 min, and $T_{2200} = T_2 = 5$ hr 33 min as seen before. Taking these terms in consideration increase the secular acceleration between 0.27% and 0.3% depending on the rheological model used and frequency dependence of the terms, justifying their inclusion. However, we note that taking into account the frequency dependence of the Q and k of these terms with the different ℓmpq generate a change in value of the secular acceleration less than 0.04% compared to a constant phase lag model, much lower than the error bar on s. Thus, calculating them at $T_2 = 5$ hr 33 min instead of their respective T_{lmpq} does not significantly impact the calculations of s.

4. Mars Interior Modeling

In this work, we compare several Martian interior models and study the sensitivity of the predicted tidal Love number k_{2200} and the secular acceleration of Phobos s to variations in the assumed fluid core size and the shear attenuation profile of Q_μ. This wide comparison aims at providing a reliable range of possible core sizes and attenuation profiles. All models considered for this study with their respective assumptions are briefly described below, and a few distinct key parameters are summarized in Table 2.

The FN models are based on Nimmo and Faul (2013) for two different mantle potential temperatures (cold and hot). The AB models are based on Khan et al. (2018) and Bagheri et al. (2019) using either the Andrade rheological model or the Burgers rheological model. The HS models are based on Samuel et al. (2019, 2021) for three different selected models of varying mantle and core properties (labeled hereafter HS1, HS2, and HS3). The TG model is based on Zharkov et al. (2017). The AR models are based on Rivoldini et al. (2011), using the bulk composition models of Mars from either G. J. Taylor (2013) (labeled hereafter TAY) or Yoshizaki and McDonough (2020) (labeled hereafter YO), with the temperature profiles from Plesa et al. (2018) (cases 85 and 111). Further details for each set of models are given in Text S1–S5 of Supporting Information S1.

The tidal Love numbers $k_{\ell mpq}$ and tidal dissipation factor $Q_{\ell mpq}$ (also referred as global Q_ℓ or tidal bulk Q in other works (e.g., Bagheri et al., 2019; Jacobson & Lainey, 2014; Nimmo & Faul, 2013)) are calculated from integrating the equations of motion when calculating the deformation of a self-gravitating planet to an external potential such as tides (e.g., Alterman et al., 1959; Takeuchi & Saito, 1972). These are integral parameters, where $k_{\ell mpq}$ is obtained from the real part of the gravity perturbation at the surface of the planet and $Q_{\ell mpq}$ from its imaginary

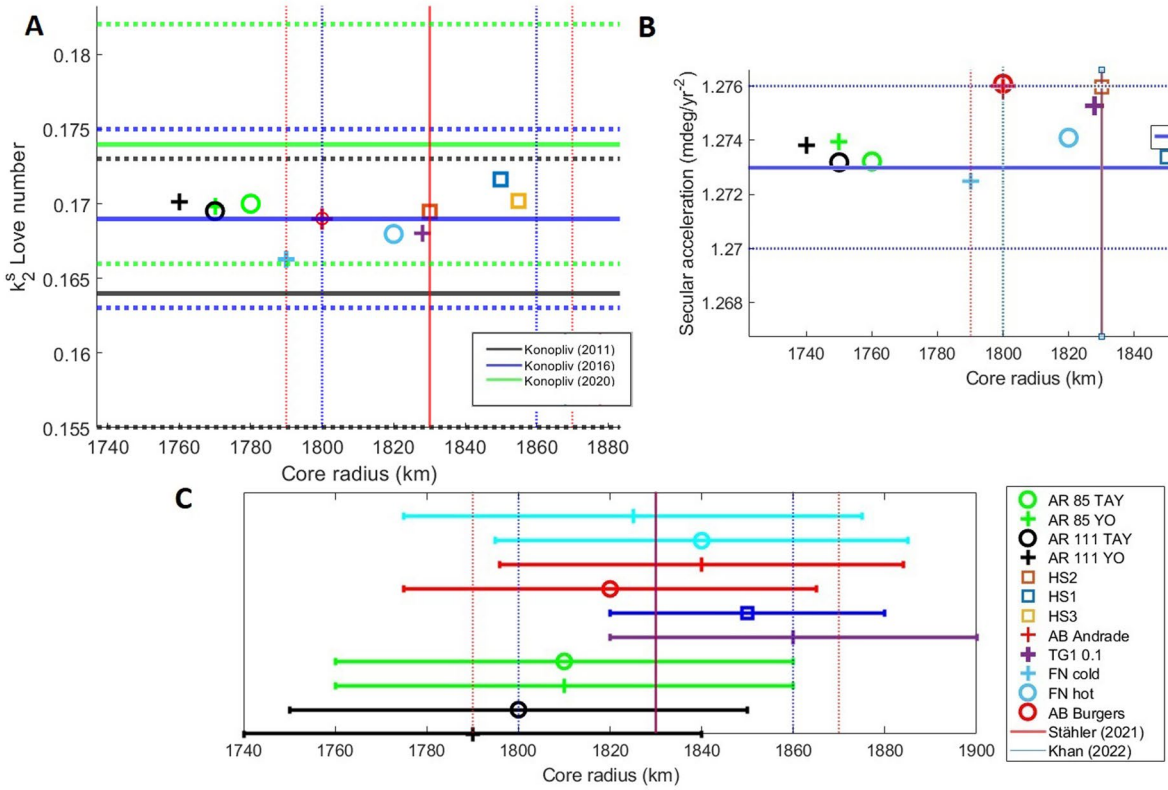

Figure 1. Top left (a): Nominal solar tide Love number k_2^s values for all models, fitting the latest value from Table 1 of $k_2^s = 0.174 \pm 0.008$ (green line indicating the mean value and dotted lines representing the uncertainty). Previous values of k_2^s from Konopliv et al. (2011) (black lines) and Konopliv et al. (2016) (blue lines) are shown for comparison, as existing models were based on them. Top right (b): Nominal s values for all models, fitting the latest measurements in Table 1 of $s = 1.273 \pm 0.003$ mdeg.yr^{-2}. Bottom (c): Range of core sizes giving k_2^s and s values matching the observations given in Table 1. Vertical lines are Mars core radius estimation from Stähler et al. (2021) (red, 1,830 ± 40 km) and Khan et al. (2022) (blue, 1,830 ± 30 km).

part. The viscoelastic properties of each model depend on the rheological model used, based on the Earth's attenuation profile (e.g., Zharkov & Gudkova, 2005) and laboratory experiments (e.g., Jackson & Faul, 2010). The rheological model chosen governs the dependence of the rigidity modulus μ to depth with pressure, temperature, and forcing period. At any given depth, the local intrinsic attenuation Q_μ due to internal friction is modeled by assuming the rigidity modulus as a complex quantity where its imaginary part depends on Q_μ. More details on the general rheological models can be seen in Jackson and Faul (2010) and how they are applied to Mars in Bagheri et al. (2019).

5. Results

5.1. k_2^s Values

Matching the tidal Love number k_2^s gives us a strong constraint on the deep interior of Mars, particularly its core size. Here, we chose to construct models that are consistent with the most recent value of k_2^s from Table 1 (see Figure 1a). While the AB models were obtained by inverting for models that fit the data, that is, the same k_2^s value for both Andrade and Burgers rheologies, for the other models, we adjusted several parameters such as the core radius or temperature profile to recreate Martian models that yield k_2^s consistent with the observations. For the core radius, this is done by varying the core radius while adjusting the core density so that the models are self-consistent in terms of the bulk density, moment of inertia, and selected bulk composition and keeping only models with a derived k_2^s consistent with its measured value. The choice of bulk composition between TA models and YO models only slightly impacts the range of possible core radii by about 10 km, as does the difference between the hot and cold thermal end-member profiles. The choice of rheology has a significant impact on the attenuation profiles with the greatest variations coming from changes in the mantle grain size (Bagheri

Table 3
Possible Core Sizes for All Martian Models Satisfying the Latest k_2^s Measurements in Table 1, Displayed on Figure 1c, With the Core Size Estimates Based on Seismic Observations by Stähler et al. (2021) and Khan et al. (2022)

Martian interior model	Core radius range from k_2^s (km)
FN cold	1,825 ± 50
FN hot	1,840 ± 45
AB Andrade	1,840 ± 44
AB Burgers	1,820 ± 45
HS	1,850 ± 30
TG	1,860 ± 40
AR - TA 85	1,810 ± 48
AR - TA 111	1,800 ± 48
AR - YO 85	1,810 ± 50
AR - YO 111	1,790 ± 50
This study's summary	1,820 ± 80
Stähler et al. (2021) estimation	1,830 ± 40
Khan et al. (2022) estimation	1,830 ± 30

et al., 2019). The range of possible core sizes from fitting k_2^s is summarized in Table 3. For most models, the core radius ranges are consistent with seismic observations of the core made by Stähler et al. (2021) and the updated study of Khan et al. (2022).

5.2. Phobos Secular Acceleration *s* Values

The secular acceleration of Phobos is sensitive to the core size of Mars through the Love numbers $k_{\ell mpq}$ (Equation 9). However, since the tidal dissipation factor $Q_{\ell mpq}$ also intervenes in Equation 16, the secular acceleration is also sensitive to mantle temperature and grain size (in the case of grain-size sensitive rheologies). The nominal secular acceleration values used for this study (Jacobson & Lainey, 2014) are shown in Figure 1b, as are the values for the models that also match the k_2^s constraint (Figure 1a). Similar to Section 5.1, core sizes around 1,820 km are compatible with the seismic observations of Stähler et al. (2021) and Khan et al. (2022).

The corresponding temperature profiles for each model are shown in Figure 2. For a given model, the very small error bars on the secular acceleration *s* strongly constrain the mantle potential temperature and its temperature profile by a few degrees if they are the only parameters changed. However, the differences between different model temperature profiles are much larger than this due to the assumptions used when building or inverting the models such as assumed lithospheric thickness or grain size. This highlights the trade-off between temperature structure and other model assumptions such as mineralogy or grain size for instance.

5.3. Dissipation Profiles

The shear attenuation Q_μ profiles at the main Phobos tide (5.55 hr) are shown in Figure 3, with an average value in the mantle a bit lower than 100 in accordance with previous works (e.g., Jacobson & Lainey, 2014; Khan et al., 2018; Nimmo & Faul, 2013; Smrekar et al., 2018). All models show similar Q_μ profiles due to the requirement to fit the secular acceleration; this was expected as the error bars are very small and degree 2 contributes more than 90% to the total acceleration. All models predict attenuation to be at its strongest just below the lithospheric lid and to decrease in the rest of the mantle toward the core-mantle boundary, although it remains

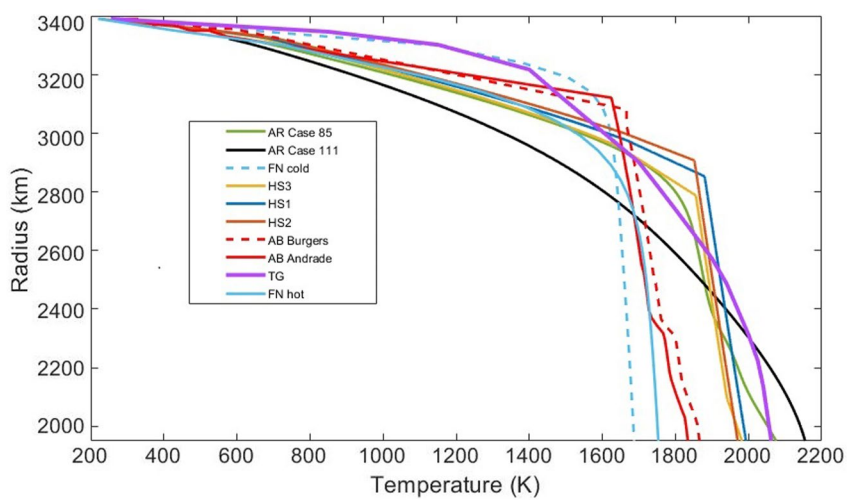

Figure 2. Temperature profiles in the Martian mantle obtained from fitting the latest measurements of the secular acceleration of Phobos in Table 1 of $s = 1.273 \pm 0.003$ mdeg.yr^{-2}.

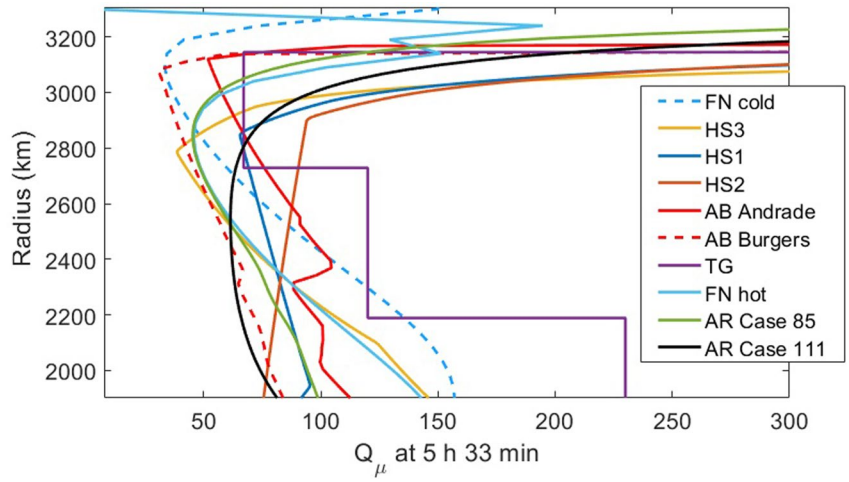

Figure 3. Q_μ profile at the main Phobos tide period (5.55 hr). Since the tidal bulk Q_{2200} is strongly constrained through the secular acceleration of Phobos, all models show a similar Q_μ profile at this frequency.

relatively significant throughout the mantle. Different bulk compositions (AR YO and AR TAY) have a negligible effect on the attenuation profiles as observed earlier (Khan et al., 2018). As a result, the profiles related to these models have been grouped by temperature profile.

6. Constraining the Attenuation of the Martian Mantle

Using Equation 16, it is possible to estimate the tidal bulk Q of Mars. As there is currently no measurement of higher degree Love numbers for Mars, we will be limiting our study to tidal degree $\ell = 2$ and neglecting the eccentricity terms. The truncated expression for the secular acceleration is as follows:

$$\frac{\mathrm{d}n}{\mathrm{d}t} = 3n^2\alpha_m \frac{3}{2}\frac{k_{2200}}{Q_{2200}}\left(\frac{r}{a}\right)^5, \tag{19}$$

with Q_{2200} the tidal bulk Q of Mars for the tidal degree $\ell = 2$ and order $m = 2$, that is, the main Phobos tide. The error on $\frac{\mathrm{d}n}{\mathrm{d}t}$ is around 0.24% based on Jacobson and Lainey (2014); the error on k_2^s is 4.5% from Konopliv et al. (2020), while the error on α_m (mainly on the mass of Phobos) is 0.18% from Pätzold et al. (2014). As k_{2200} is not directly measured and the difference between k_{2200} and k_2^s is significantly lower than the error on k_2^s, we will assume the uncertainty on k_{2200} is of the same magnitude as the error on k_2^s. As indicated in Section 3.2, for a given interior model of Mars the value of k_2^s differs from k_{2200} by about 0.5%–1%. Because this dispersion is significantly lower than the error on k_2^s (contrary to when calculating the secular acceleration, where this dispersion is much larger than the error on s) and as the considered models in this study do not yield a unique k_2^s value, for the purpose of estimating Q_{2200} only will we take k_2^s and k_{2200} to be equal. Because we truncated the secular acceleration of Phobos at degree 2, we must also take into account the higher degree terms as error terms for our calculations. However, our models were constructed to fit the whole secular acceleration. Therefore, if only fitting the secular acceleration up to degree 2 with the contribution for the Q_{2200} value used, the actual error on Q_{2200} will only be due to the dispersion in the value of the degree-2 term for all our models. As the contribution of the degree-2 terms to the secular acceleration varies by only ±1% between the different models, we will add this ±1% value to the error budget for Q_{2200}. For a mean value of $k_{2200} = 0.174$, this gives us an estimation of $Q_{2200} = 93.0 \pm 8.40$ with a relative error ΔQ_{2200} of about 9%, compatible with previous estimations of Jacobson and Lainey (2014) and Khan et al. (2018) who found $Q_2 = 99.5 \pm 4.9$ and $Q_2 = 95 \pm 10$, respectively. This error bar is significantly larger than the amplitude of the eccentricity terms (less than 0.3% total contribution on s), justifying our assumptions.

This bulk Q_{2200} is the attenuation of Mars as a whole felt by Phobos. However, as shown in Figure 3, the attenuation in the Martian mantle is far from homogeneous and varies considerably with depth depending on the selected model. To illustrate these variations in the Martian interior, it is more relevant to consider the local Q_μ,

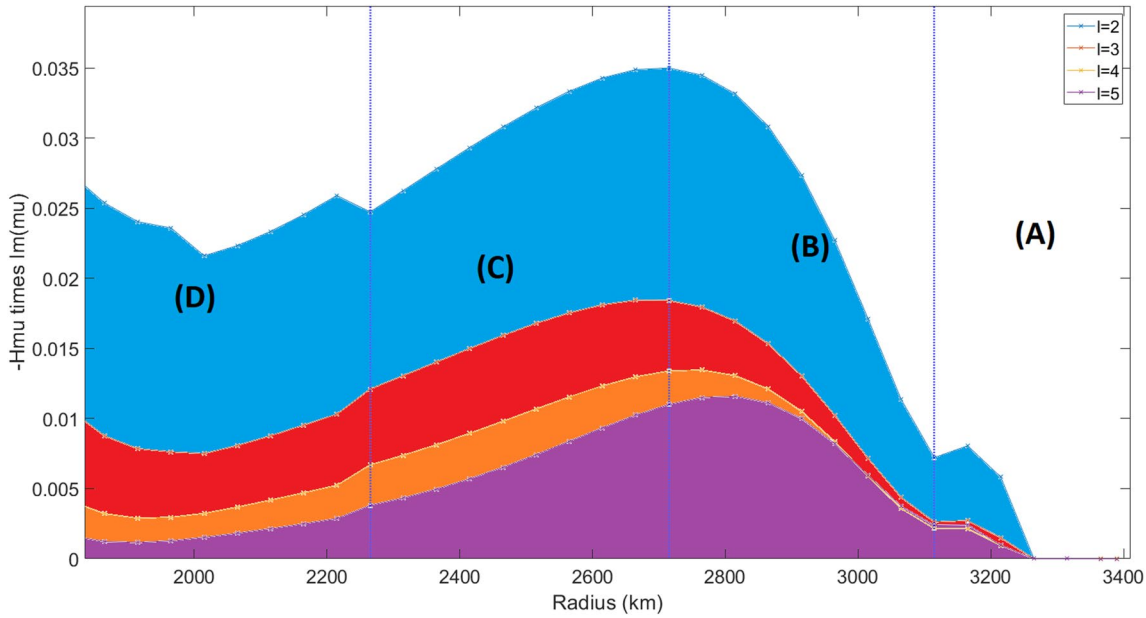

Figure 4. Sensitivity parameter H_μ multiplied by the imaginary part of the shear modulus Im(μ) (right-hand side term in Equation 20) in the Martian model for the FN hot model, for degree 2 up to 5. The surface area below each curve represents the dissipation in each layer of the Martian interior that contributes to the bulk tidal dissipation rate k_2/Q. Mantle subdivisions are indicated with blue lines (details in text). This takes into account the actual value of Q_μ in the mantle to show that for this model, dissipation is actually stronger in the upper layer of the lower mantle (C area) due to its lower Q_μ compared to the lower layer of the lower mantle (D area), and it is clearly visible that the lithosphere has a very limited impact and almost none for the crust.

hereafter denoted $Q_\mu(i, \omega)$, to highlight its depth and frequency dependence, where i is an index for the interior part considered (to be quantified in the following section) and ω the frequency at which this local Q_μ is computed. Each layer of the Martian interior with local attenuation $Q_\mu(i, \omega)$ will contribute to the global bulk Q_{2200}. This can be quantified so as to separate the contribution of each part of the Martian interior.

6.1. Contribution of the Different Parts of the Interior

The contribution to the tidal dissipation within Mars from the different parts of the Martian interior can be estimated through the radial sensitivity function H_μ to shear modulus μ. This parameter can be directly linked to the ratio k_ℓ/Q_ℓ (cf., Equation 33 of Tobie et al. [2005]) as follows:

$$\frac{(2\ell+1)r}{4\pi G}\frac{k_\ell}{Q_\ell} = \int_0^r H_\mu(z)\mathrm{Im}(\mu(z))\mathrm{d}z, \tag{20}$$

where r is the radius of Mars, ℓ the tidal degree, Im($\mu(z)$) is the imaginary part of the shear modulus μ, z the integration variable with respect to depth, and G the gravitational constant. This is particularly relevant to our study as these terms are directly used in the expression for the secular acceleration (Equation 16).

Equation 20 is similar to the works of Zharkov and Gudkova (2005) and Zharkov et al. (2017) where the authors estimated the contribution of each layer in the Martian interior to the bulk tidal dissipation factor Q_{2200}. Rather than only comparing the contribution of each layer for all models to the bulk tidal dissipation factor, we prefer to compare the amount of dissipation occurring within each layer of the Martian mantle.

We divide the Martian interior into four parts: crust and lithosphere (A), the olivine-dominated upper mantle (B), and the lower mantle which is sub-divided into an olivine layer (C) and a bottom layer consisting of the high-pressure polymorphs of olivine, wadsleyite and ringwoodite (D). In Figure 4 the contribution to tidal dissipation in these 4 parts of the Martian interior is shown for the FN hot model. We observe that for increasing spherical harmonic degree, tidal dissipation becomes more sensitive to shallower regions. While the relative contribution to the degree-2 terms is dominated by the lower mantle, degree-4 and -5 terms are mostly governed

Table 4
Contribution to the Tidal Dissipation Rate of the 4 Parts of the Martian Interior Models for Degree 2

	Relative contribution of Martian interior model subdivisions			
Martian interior model	(A)	(B)	(C)	(D)
AR - TA 85	3.79%	26.84%	33.87%	35.5%
AR - TA 111	1.65%	17.32%	37.98%	44.05%
AR - YO 85	2.79%	25.57%	36.19%	35.45%
AR - YO 111	1.69%	17.73%	38.17%	42.41%
FN hot	1.40%	24.23%	40.81%	33.56%
TG	1.26%	18.9%	55.37%	24.47%
Mean	1.99 ± 0.33%	21.74 ± 1.41%	41.49 ± 2.85%	34.78 ± 2.43%

Note. (A) is crust + lithosphere, (B) is upper mantle, (C) is top of the lower mantle, and (D) is bottom of the lower mantle. Error bars in the mean values are estimated from the dispersion between all models. Only large core sizes were kept for the AR models. As the AB models were constructed by inversion to fit observations and because of the parametrization used for computing the HS models, the H_μ could not be calculated for them.

by the dissipation in the upper mantle. The lithosphere and crust do not contribute significantly to the tidal dissipation since dissipation is smaller there (i.e., higher Q_μ) than in the deeper mantle.

Since tidal degree 2 represents more than 90% of the total secular acceleration of Phobos for all models, we focus our comparative efforts between our models on this single degree. Table 4 summarizes the relative contribution of each part of the Martian interior to the degree 2 tidal dissipation between the models for which the H_μ functions could be computed, depending on how they were constructed. From Table 4, we can make the following observations:

- Temperature appears to have the largest effect, as indicated by the models AR-TA/YO 85/111;
- the role of composition is minor;
- for all considered models, the relative contribution from the various layers is similar, with dissipation being concentrated in the lower mantle.

6.2. Linking Tidal and Seismic Constraints

As seen before, the tidal bulk Q_{2200} is strongly constrained by the secular acceleration of Phobos. Using the Q_μ profile deduced at tidal frequencies, we can try to predict the possible Q_μ profiles in the Martian interior at seismic frequencies depending on the rheological model and the frequency dependence of Q_μ. Because of the different rheology and thermal models used for the Martian interior, we can expect differences to appear as they directly impact the shear attenuation Q_μ. We reemphasize here that the local intrinsic attenuation is given by Q_μ, with the layer i and its forcing frequency ω given as arguments. The integral parameter Q_{2200} is the tidal bulk dissipation factor, representing the attenuation of Mars as a whole with its forcing period given by Equation 18 and being also sensitive to gravity and inertial effects (see also Bagheri et al. [2019]).

The seismic Q_μ profiles at 1s are plotted in Figure 5. Several models are clipped at shallower depth, where the attenuation felt by seismic waves is not related to temperature or other material properties as in the rest of the Martian mantle. At seismic frequencies, some models have an average Q_μ between 100 and 200 in the mantle while others tend more toward a Q_μ of about 1,000. Almost all models still predict attenuation to be at its strongest just below the lithospheric lid, but attenuation at the core-mantle boundary is also strong and even stronger in a few cases.

As illustrated by Figure 5, the possibility of distinguishing the various models with seismic measurements also depends on the depth of these measurements. Because the lower mantle is more constrained from tidal measurements than the shallower parts (as seen in Figure 4 and Table 4), a measurement of the seismic quality factor Q_μ in the lower mantle would provide a stronger constraint as these parts of the mantle contribute more to the bulk tidal Q values than shallower layers.

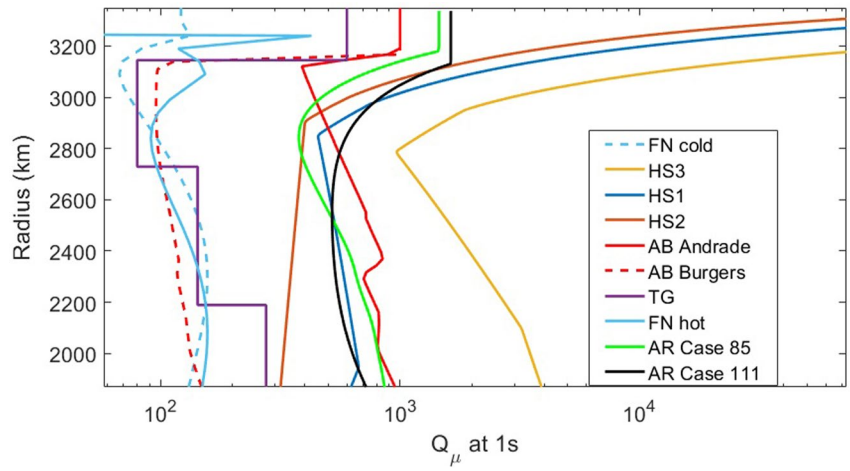

Figure 5. Q_μ profile at 1s. Most models predict the strongest attenuation to occur just below the lithosphere. Because of the different thermal structure and grain sizes assumed for the models, the predictions for the Q_μ profiles show large differences between models, with some models having an average Q_μ in the mantle in the hundreds while the others are near 1,000.

One can attempt to estimate how much such seismic measurements would be able to constrain our knowledge of the interior of Mars using the H_μ functions and contributions of the different parts of the Martian interior. If we assume that we have a measurement $Q_{\mu,meas}$ from seismic observations of Q_μ at a given depth i (simplified here by either area (A), (B), (C), or (D) as defined in Section 6.1):

$$Q_{\mu,meas}\,(i,\omega_{seismic}) = Q_\mu\,(i,\omega_{seismic}) \tag{21}$$

where i and ω are used as a reminder that this is a local, frequency-dependent quality factor unlike the bulk tidal $Q_{\ell mpq}$ which is a global parameter only dependent on frequency. From laboratory experiments, the frequency dependence of Q_μ can be quantified by the parameter α (e.g., Bagheri et al., 2019; Jackson & Faul, 2010; Nimmo & Faul, 2013):

$$Q_\mu(i,\omega) \propto \omega^\alpha \tag{22}$$

with ω the forcing angular frequency. Using this relation, we can extrapolate the attenuation at the tidal periods of Phobos from the seismic measurements:

$$Q_\mu\,(i,\omega_{tidal}) = \left[Q_\mu\,(i,\omega_{seismic})\right]\left(\frac{\omega_{tidal}}{\omega_{seismic}}\right)^\alpha \tag{23}$$

Note here that for simplification, we are assuming a single theoretical α value with no error bars. If using a measurement of α with uncertainties, this would create additional terms and would impact subsequent equations. From Equation 20, we know that the tidal bulk $Q_{\ell mpq}$ can be rewritten as a sum of the contribution of the local Q_μ in the different parts of the Martian interior. Hence, we can rewrite Equation 20 by introducing weights β such as the following:

$$\frac{1}{Q_{\ell mpq}} = \sum_{j=A,B,C,D} \beta_i \frac{1}{Q_\mu\,(j,\omega_{\ell m})}, \tag{24}$$

Here, the β_i are functions of the H_μ, which depend on the rheology. $\omega_{\ell m}$ is the tidal frequency corresponding to the degree ℓ and order m of the considered tide. By taking into account the seismic measurements with Equation 23, we can define a weighted average $Q_{\mu,unc.}$ representing the weighted attenuation in the mantle unconstrained by the seismic measurements $Q_\mu(i,\omega_{seismic})$:

$$Q^{-1}_{\mu,unc.}\,(r,\omega_{\ell m}) = \frac{1}{\sum_{j\neq i}\beta_j}\left(Q^{-1}_{\ell mpq} - \beta_i\left(Q^{-1}_\mu\,(i,\omega_{\ell m})\right)\right) \tag{25}$$

Hence, from a seismic measurement of the attenuation in the interior of Mars $Q_{\mu,meas}$, it is possible to estimate what is the attenuation in the rest of the Martian interior $Q_{\mu,unc.}$. Depending on the error $\Delta Q_{\mu,meas}(i, \omega_{seismic})$ on $Q_{\mu,meas}(i, \omega_{seismic})$, this can be used to distinguish between the Martian interior structures and rheological models based on their expected attenuation profiles.

Details about the propagation of the error $\Delta Q_{\mu,meas}(i, \omega_{seismic})$ are given in Appendix B. If we apply this error propagation to a notional measurement of $Q_{\mu,meas} = 2{,}000 \pm 500$ in the lower mantle (D) of Mars at 1s for $\alpha = 0.33$, we can estimate having $Q_{\mu,tidal}\left(D, \omega_{T_2}\right) = 76 \pm 19$ in the lower mantle with Equation 22. Using Equation 25 and Table 4, we derive $Q_{\mu,unc}\left(r, \omega_{T_2}\right) = 107.2 \pm 37.5$ in the rest of the Martian mantle, translating into $Q_{\mu,unc}(r, \omega_{1s}) = 2{,}820 \pm 987$ at seismic frequencies, which is enough to make all models with $\alpha = 0.33$ and attenuation at seismic frequencies $Q_{\mu,unc}(r, \omega_{1s})$ lower than 1,000 in the rest of the Martian mantle (areas (B) and (C)) unlikely to be representative of Mars.

One must note that the actual value of the frequency dependence α directly impacts this estimation, while α can also be constrained if the seismic measurements are accurate enough to distinguish between the models as shown in Figure 5.

6.3. Other Nontidal Constraints

Besides seismic measurements and tidal constraints, there are other possible ways to distinguish between the models, which we will discuss in the following.

6.3.1. Elastic Lithospheric Thickness

The elastic lithosphere thickness is considered a proxy for the thermal state of the lithosphere and can be approximated by the mechanical thickness, which is always greater or equal to the elastic thickness (Plesa et al., 2018). Given a rheological model, the latter can be used to estimate the depth below which rocks lose their mechanical strength and the corresponding temperature associated with ductile failure. The deflection of the surface below the north polar cap on Mars was used to estimate an elastic thickness of the lithosphere T_e of values greater than 330 km (Broquet et al., 2020). At the south pole of Mars, T_e is estimated to be larger than 200 km (Broquet et al., 2021). In comparison, thermal evolution modeling fitting these measurements with a strain rate between $10^{-14}s^{-1}$ and $10^{-17}s^{-1}$ results in an average T_e for the Martian lithosphere of about 275 ± 10 km, for a temperature at the base of the elastic layer, respectively, between 1,232 and 1,090 K (e.g., Grott & Breuer, 2008; Plesa et al., 2018).

Results of the comparison between the temperature profiles of our models and the temperature needed at the base of the elastic layer to match polar caps estimates of the elastic thickness of the lithosphere are plotted in Figure 6. We can see that some models are too hot, indicating a much thinner average elastic thickness that might be incompatible with the small deflection beneath the polar caps of Mars. The temperature gradients needed in the lithosphere to fit the elastic thickness of the lithosphere at both the north pole and south pole ranges show good compatibility with the inverted geotherms of the upper mantle of Mars constrained by seismic observations in Khan et al. (2021), favoring again colder models. One must, however, note that there are several complications associated with the elastic thickness estimates and the calculation from numerical thermal evolution models. First, strain rates are only estimations and may be in fact much smaller than the values of $10^{-14}s^{-1}$ and $10^{-17}s^{-1}$ that were used here. This will lead to much thinner elastic thickness values from numerical thermal evolution models that seem at odds with the elastic thickness estimates. On the other hand, the polar cap load may not be yet at elastic equilibrium but rather in a transient state, in which case the elastic lithosphere thickness estimates would be smaller (Broquet et al., 2020). Whether these complications will lead to a larger number of models compatible with the elastic thickness estimates or whether only a small number of models will be able to fit the observations, remains to be investigated in future studies.

6.3.2. Chandler Wobble

The frequency of the Chandler wobble P_{CW} for our models is calculated under the assumption of a triaxial body with a fluid core (Konopliv et al., 2020; Zharkov et al., 2009):

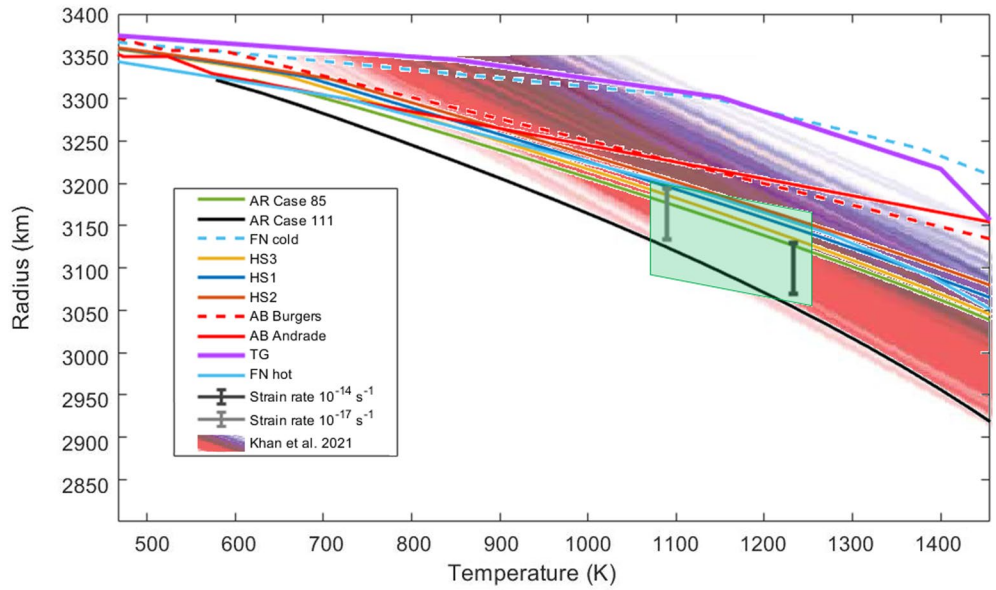

Figure 6. Constraints from the elastic thickness on the temperature profiles, for strain rates between $10^{-14}s^{-1}$ and $10^{-17}s^{-1}$ based on Grott and Breuer (2008) and Plesa et al. (2018) and comparison with the upper mantle inversions from seismic waves from Khan et al. (2021). The green area delimited by the vertical black segments highlights the possible temperatures at the base of the elastic layer from thermal modeling (e.g., Plesa et al., 2018) that are consistent with the observed lithospheric flexure from Broquet et al. (2020) and Broquet et al. (2021). The red band from Khan et al. (2021) are models with a thermal lithosphere thickness between 400 and 500 km from geophysical inversions, while the blue band are between 500 and 600 km from seismic inversions. Hotter models do not fit the inferred elastic thickness. Colder models with a higher average elastic thickness are capable of fitting the polar elastic thickness.

$$P_{CW} = \frac{P_{CW}^{rigid}\left(1 - \left(\frac{A_c B_c}{AB}\right)^{\frac{1}{2}}\right)}{1 - \frac{k_2}{k_0}}, \tag{26}$$

where A and B are the equatorial moments of Mars, A_c and B_c the equatorial moments of the core, $P_{CW}^{rigid} = \frac{2\pi}{\omega_{spin}}\left(\frac{AB}{(C-A)(C-B)}\right)^{\frac{1}{2}}$, $k_0 = \frac{3J_2 g}{\omega_{spin}^2 r}$, g is the surface acceleration, J_2 the oblateness coefficient, ω_{spin} is the body spin rate, r the average radius of Mars, and C is the polar moment of inertia of Mars. For simplicity, we assume axisymmetry of the Martian core as triaxiality only has a small impact on the Chandler wobble period (Konopliv et al., 2020), and use the physical parameters representative of Mars provided in Konopliv et al. (2020).

Figure 7 shows the period P_{CW} of the Chandler wobble for our models compared to the Konopliv et al. (2020) measurements, with for reference the dispersion of the Love number k_2^s from Figure 1. While all of our models fit the Love number k_2^s value, they do not exactly fit the Chandler wobble period estimate. The models with the closest values would suggest a frequency dependence of Q to be close to $\alpha = 0.15$–0.4 (see Table 2) but some models within this range of α are still outside of the measured Chandler wobble period. This is because while the Chandler wobble period is sensitive to α, there are also other influences at play such as rheology models or grain size. Figure 7 therefore only indicates likely values rather than a direct determination of α which would require P_{CW} to be inverted together with other tidal constraints to construct a more complete Martian model.

7. Conclusion

Measurements of the Love number k_2 of Mars and the secular acceleration of Phobos s provide strong constraints on the interior structure of Mars. While k_2 is mostly sensitive to the rigidity structure of Mars and the size of its core, the secular acceleration s is strongly dependent on the thermal structure of the Martian mantle. When using

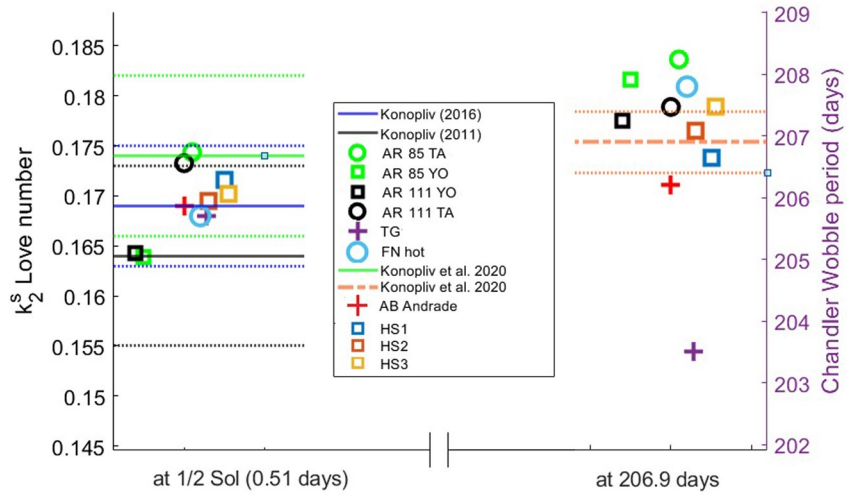

Figure 7. Comparison of the k_2^s (left side) and P_{CW} values (right side) for our different models with the Martian measurements. Dotted lines indicate the error bars for their respective k_2^s and P_{CW} measurements based on colors. All models fit the k_2^s measurements (Figure 1) but not all of them fit the Chandler Wobble frequency measured in Konopliv et al. (2020), providing an additional constraint on the rheology of the Martian interior. Dotted lines on the left indicates k_2 values used in this study given in Table 1, while dotted lines on the right indicate the Chandler Wobble period range given in Konopliv et al. (2020).

constraints on k_2 and s together with a range of different models, we can place bounds on the Martian core size and temperature profiles in the Martian interior. Using an ensemble of models also makes our deductions more robust, as our results are less sensitive to assumptions (e.g., rheology and mineralogy) made by any individual model.

We also explored possible ways to distinguish between the constructed models, such as elastic thickness, laboratory experiments, Chandler wobble measurements, and more specifically a synergy with seismic wave measurements and the InSight mission. From these constraints, we find that Martian models with larger core sizes and colder temperature profiles under the lithosphere are favored. We also determine how the attenuation of Mars at tidal periods is distributed in its interior and can use it to link local potential seismic measurements of the Martian attenuation to the attenuation in the rest of the Martian mantle.

A shortcoming of our approach is that we assumed that all of the secular acceleration of Phobos is due to tidal dissipation. This is not necessarily true, as other nontidal effects can also create a secular acceleration on the Martian moon. For instance, a time-dependent gravity field coefficient J_2 would have a similar effect, similar to the glacial isostatic adjustment on Earth or seasonal polar cap melting.

The recent measurements of the Chandler wobble frequency could also be used directly as an additional fitting parameters in our models, as we have shown that it is effective at constraining the range of possible tidal dissipation Q through its frequency dependence α, as its frequency of hundreds of days is well-separated from the tidal measurements around tens of hours for the solar tides and the main Phobos tide frequency.

The results of this study are compatible with the direct detection of deep seismic waves Stähler et al., 2021) by the seismometer of the InSight mission (Banerdt et al., 2020; Lognonné et al., 2019, 2020) (see Table 3), and attenuation of seismic waves in the deep interior of Mars would help distinguish between our models. Additional constraints on the Martian core may also be provided from radio measurements by the RISE instrument (Rotation and Interior Structure Experiment, Folkner et al., 2018); the upcoming data together with the tidal constraints of this work will allow even more robust and accurate predictions of the thermal, rheological, and compositional state of Mars.

Appendix A: Eccentricity Terms for the Calculation of the Secular Acceleration

For degree 2, the terms in order 1 in eccentricity and order 0 in inclination correspond to $\ell mpq = 2201$, $\ell mpq = 220\text{-}1$, $\ell mpq = 2011$, and $\ell mpq = 201\text{-}1$, giving the same F(i*) functions but the additional G(e*) functions:

$$\begin{aligned} F_{\ell mp=220} &= 3 \\ G_{\ell pq=201} &= \frac{7e}{2} \\ G_{\ell pq=20-1} &= -\frac{e}{2} \\ F_{\ell mp=201} &= -\frac{1}{2} \\ G_{\ell pq=211} &= \frac{3e}{2} \\ G_{\ell pq=21-1} &= \frac{3e}{2} \end{aligned} \tag{A1}$$

resulting in the following tidal potential terms:

$$V_{2201} = \frac{21e}{8}\frac{Gm^*r^2}{a^{*3}}\left(1-\cos^2\theta\right)\cos\left(2\omega^* + M^* + 2\Omega^* - 2\phi\right) \tag{A2}$$

$$V_{220-1} = -\frac{3e}{8}\frac{Gm^*r^2}{a^{*3}}\left(1-\cos^2\theta\right)\cos\left(2\omega^* + 3M^* + 2\Omega^* - 2\phi\right) \tag{A3}$$

$$V_{201-1} = -\frac{3e}{8}\frac{Gm^*r^2}{a^{*3}}\left(3\cos^2\theta - 1\right)\cos M^* \tag{A4}$$

$$V_{2011} = -\frac{3e}{8}\frac{Gm^*r^2}{a^{*3}}\left(3\cos^2\theta - 1\right)\cos -M^* \tag{A5}$$

As we are studying secular effects due to a phase lag, we must also consider higher eccentricity terms for $\ell mpq = 2200$. This is not the case for $\ell mpq = 2010$ since this potential is not affected by the phase lag and therefore will not impact the secular acceleration of Phobos as seen in Equation 12. By including higher terms in eccentricity in F_{220}, V_{2200} becomes

$$V_{2200} = \frac{3\left(2-5e^2\right)}{8}\frac{Gm^*r^2}{a^{*3}}\left(1-\cos^2\theta\right)\left(\cos\left(2\omega^* + 2M^* + 2\Omega^* - 2\phi\right)\right), \tag{A6}$$

These potentials can also be found in the work of Boué and Efroimsky (2019) where the authors studied a two-body problem where the Keplerian elements evolution is governed by tides. In this case the evolution of the semimajor axis a* is given by the following equation:

$$\begin{aligned} \left(\frac{da^*}{dt}\right)_{\ell=2} = &-3\,a^*\,n\,\alpha_m\left(\frac{r}{a^*}\right)^5\left(k_{2200}\,\epsilon_{2200}\right) \\ &+ 15e^{*2}\,a^*\,n\,\alpha_m\left(\frac{r}{a^*}\right)^5\left(k_{2200}\,\epsilon_{2200}\right) \\ &- \frac{9e^{*2}}{8}\,a^*\,n\,\alpha_m\left(\frac{r}{a^*}\right)^5\left(k_{201-1}\,\epsilon_{201-1}\right) \\ &- \frac{9e^{*2}}{8}\,a^*\,n\,\alpha_m\left(\frac{r}{a^*}\right)^5\left(k_{2011}\,\epsilon_{2011}\right) \\ &- \frac{3e^{*2}}{8}\,a^*\,n\,\alpha_m\left(\frac{r}{a^*}\right)^5\left(k_{220-1}\,\epsilon_{220-1}\right) \\ &- \frac{441e^{*2}}{8}\,a^*\,n\,\alpha_m\left(\frac{r}{a^*}\right)^5\left(k_{2201}\,\epsilon_{2201}\right) \end{aligned} \tag{A7}$$

which is derived from Equation 193 of Boué and Efroimsky (2019). When taking into account eccentricity, two changes must be taken into account when calculating $k_{\ell mpq}$ and $Q_{\ell mpq}$. The period at which the last four $k_{\ell mpq}$ and $Q_{\ell mpq}$ are calculated is no longer related to the synodic period T_1 of Phobos and instead must be calculated at the period given by Equation 18.

As we consider the potential terms with order 1 in eccentricity, their period $T_{\ell mpq}$ is not directly linked to the synodic period of Phobos; hence, their deformation pattern is also not directly linked to the geometric lag angle

$\gamma_{\ell mpq}$, which we recall is the geometric angle between the tidal bulge and the position of Phobos on its orbit. This means that Equation 13 is no longer valid, thus our use in Equation A7 of the phase lag $\epsilon_{\ell mpq}$ instead as done in Kaula (1964) and Boué and Efroimsky (2019). When converting the $\epsilon_{\ell mpq}$ into $Q_{\ell mpq}$, one must pay close attention to the signs of each $\epsilon_{\ell mpq}$. While all $Q_{\ell mpq}$ are definite positive by convention, their corresponding $\epsilon_{\ell mpq}$ is the same sign as $(\ell - 2p + q)n - \dot{\phi}$ which is the denominator in Equation 18 (Boué & Efroimsky, 2019). The $\epsilon_{\ell mpq}$ can therefore be either positive or negative depending on the binary system considered. In the case of Phobos and Mars, for the studied potentials and respective ℓmpq values, this term is always positive; therefore all $\epsilon_{\ell mpq}$ are positive like all $Q_{\ell mpq}$ values. Taking this into consideration, Equation A7 can be expressed in terms of $Q_{\ell mpq}$ using Equation 14:

$$\begin{aligned}\dot{a^*} = \left(\frac{da^*}{dt}\right)_{\ell=2} &= -3\,a^*\,n\,\alpha_m\left(\frac{r}{a^*}\right)^5\left(\frac{k_{2200}}{Q_{2200}}\right)\\ &+ 15e^{*2}\,a^*\,n\,\alpha_m\left(\frac{r}{a^*}\right)^5\left(\frac{k_{2200}}{Q_{2200}}\right)\\ &- \frac{9e^{*2}}{8}\,a^*\,n\,\alpha_m\left(\frac{r}{a^*}\right)^5\left(\frac{k_{201-1}}{Q_{201-1}}\right)\\ &- \frac{9e^{*2}}{8}\,a^*\,n\,\alpha_m\left(\frac{r}{a^*}\right)^5\left(\frac{k_{2011}}{Q_{2011}}\right)\\ &- \frac{3e^{*2}}{8}\,a^*\,n\,\alpha_m\left(\frac{r}{a^*}\right)^5\left(\frac{k_{220-1}}{Q_{220-1}}\right)\\ &- \frac{441e^{*2}}{8}\,a^*\,n\,\alpha_m\left(\frac{r}{a^*}\right)^5\left(\frac{k_{2201}}{Q_{2201}}\right)\end{aligned} \tag{A8}$$

Assuming that all of the secular acceleration of Phobos is due to tides, we can use Kepler's laws as follows:

$$\frac{1}{n}\frac{dn}{dt} = -\frac{3}{2}\frac{\dot{a^*}}{a^*} \tag{A9}$$

Therefore, the second-degree terms for the secular acceleration of Phobos when taking eccentricity into account are as follows:

$$\begin{aligned}\left(\frac{1}{n}\frac{dn}{dt}\right)_{\ell=2} &= 3\,n\,\alpha_m\left(\frac{r}{a^*}\right)^5\left(\frac{3}{2}\frac{k_{2200}}{Q_{2200}}\right)\\ &- 15e^{*2}\,n\,\alpha_m\left(\frac{r}{a^*}\right)^5\left(\frac{3}{2}\frac{k_{2200}}{Q_{2200}}\right)\\ &+ \frac{9e^{*2}}{8}\,n\,\alpha_m\left(\frac{r}{a^*}\right)^5\left(\frac{3}{2}\frac{k_{201-1}}{Q_{201-1}}\right)\\ &+ \frac{9e^{*2}}{8}\,n\,\alpha_m\left(\frac{r}{a^*}\right)^5\left(\frac{3}{2}\frac{k_{2011}}{Q_{2011}}\right)\\ &+ \frac{3e^{*2}}{8}\,n\,\alpha_m\left(\frac{r}{a^*}\right)^5\left(\frac{3}{2}\frac{k_{220-1}}{Q_{220-1}}\right)\\ &+ \frac{441e^{*2}}{8}\,n\,\alpha_m\left(\frac{r}{a^*}\right)^5\left(\frac{3}{2}\frac{k_{2201}}{Q_{2201}}\right)\end{aligned} \tag{A10}$$

From Equation 18, the periods of k_{201-1} and k_{2011} are the same, leading to a further simplification:

$$\begin{aligned}\left(\frac{1}{n}\frac{dn}{dt}\right)_{\ell=2} &= 3\,n\,\alpha_m\left(\frac{r}{a^*}\right)^5\left(\frac{3}{2}\frac{k_{2200}}{Q_{2200}}\right)\\ &- 15e^{*2}\,n\,\alpha_m\left(\frac{r}{a^*}\right)^5\left(\frac{3}{2}\frac{k_{2200}}{Q_{2200}}\right)\\ &+ \frac{9e^{*2}}{4}\,n\,\alpha_m\left(\frac{r}{a^*}\right)^5\left(\frac{3}{2}\frac{k_{2011}}{Q_{2011}}\right)\\ &+ \frac{3e^{*2}}{8}\,n\,\alpha_m\left(\frac{r}{a^*}\right)^5\left(\frac{3}{2}\frac{k_{220-1}}{Q_{220-1}}\right)\\ &+ \frac{441e^{*2}}{8}\,n\,\alpha_m\left(\frac{r}{a^*}\right)^5\left(\frac{3}{2}\frac{k_{2201}}{Q_{2201}}\right)\end{aligned} \tag{A11}$$

from which Equation 17 is derived.

Appendix B: Error Calculations for Section 6.2

One can attempt to estimate how much seismic measurements would be able to constrain our knowledge of the interior of Mars using the H_μ functions and contributions of the different parts of the Martian interior. If we assume that we have a measurement from seismic observations of Q_μ at a given depth i (simplified here by either area (A), (B), (C), or (D) as defined in Section 6.1) with an uncertainty on the measurement $\Delta Q_{\mu,meas}$:

$$Q_{\mu,meas}\left(i,\omega_{seismic}\right)=Q_\mu\left(i,\omega_{seismic}\right)\pm\Delta Q_{\mu,meas}\left(i,\omega_{seismic}\right) \tag{B1}$$

where i and ω are used as a reminder that this is a local, frequency-dependent quality factor unlike the bulk tidal $Q_{\ell mpq}$ which is a global parameter only dependent on frequency. Assuming the frequency dependence of Q_μ to α given by Equation 22, we can extrapolate the attenuation at the tidal periods of Phobos from the seismic measurements:

$$\begin{aligned}Q_\mu\left(i,\omega_{tidal}\right)=&\left[Q_\mu\left(i,\omega_{seismic}\right)\right]\left(\frac{\omega_{tidal}}{\omega_{seismic}}\right)^\alpha\\&\pm\left[\Delta Q_{\mu,meas}\left(i,\omega_{seismic}\right)\right]\left(\frac{\omega_{tidal}}{\omega_{seismic}}\right)^\alpha\end{aligned} \tag{B2}$$

As before, we are here assuming a single theoretical α value with no error bars. If using a measurement of α with uncertainties, this would create additional terms and would impact subsequent equations.

The error $\Delta Q_{\mu,unc.}\left(r,\omega_{\ell m}\right)$ on the weighted unconstrained average $Q_{\mu,unc.}\left(r,\omega_{\ell m}\right)$, expressed in Equation 25, can be derived using Equation 24:

$$\begin{aligned}\Delta Q^{-1}_{\mu,unc.}\left(r,\omega_{\ell m}\right)=&\frac{1}{\Gamma}\Delta\left(\sum_{j\neq i}\beta_j\right)\\&+\frac{1}{\Gamma^2}\left(\Delta Q^{-1}_{\ell mpq}-\beta_i\Delta\left(Q^{-1}_\mu\left(i,\omega_{\ell m}\right)\right)-\left(Q^{-1}_\mu\left(i,\omega_{\ell mpq}\right)\right)\Delta\beta_i\right),\end{aligned} \tag{B3}$$

where $\Gamma=\left(Q^{-1}_{\ell mpq}-\beta_i Q^{-1}_\mu\left(r,\omega_{\ell m}\right)\right)$ is the attenuation in the Martian interior unconstrained by the seismic measurements and $\Delta\left(Q^{-1}_\mu\left(i,\omega_{\ell m}\right)\right)$ is the second term in the right member of Equation B2.

Depending on the depth of the seismic measurements, the error $\Delta Q_{\mu,unc.}\left(r,\omega_{\ell m}\right)$ might be ill-defined. If the measured $Q_\mu(i,\omega_{seismic})$ and hence the extrapolated $Q_\mu\left(i,\omega_{\ell m}\right)$ is too small (meaning strong dissipation), the Γ term becomes very large as this means too much dissipation is concentrated in this local area, hence requiring extremely high $Q_{\mu,j\neq i}$ in the other parts of the Martian interior. If the relative weight β_i is small (meaning the measurements are sensitive to only the crust or the lithosphere), the error $\Delta Q_{\mu,meas}(i,\omega_{seismic})$ does not really matter as the seismic measurements fails to constrain a significant contribution of the dissipation in the Martian interior. In that case, the best estimator for the attenuation in the Martian is from the tidal bulk $Q_{\ell mpq}$, except if $Q_\mu(i,\omega_{seismic})$ is extremely small as mentioned above.

If the previous cases are avoided, then we can estimate how strong the impact of the seismic measurements is on the error bars $\Delta Q_{\mu,unc.}\left(r,\omega_{\ell m}\right)$ of the unconstrained Martian attenuation $Q_{\mu,unc.}\left(r,\omega_{\ell m}\right)$. Because only the degree 2 Love number k has been measured, we will limit our analysis to $\ell=2$. From Table 4, the term $\Delta\beta_i$ is limited to around 4% between our models. The term $\Delta\left(Q^{-1}_{\mu,tidal}\left(i,\omega_{\ell m}\right)\right)$ is directly linked to the error on the seismic measurement $\Delta Q_{\mu,meas}(i,\omega_{seismic})$ using Equation B2:

$$\Delta\left(Q^{-1}_\mu\left(i,\omega_{\ell m}\right)\right)=\frac{\Delta Q_{\mu,meas}\left(i,\omega_{seismic}\right)}{Q^2_{\mu,meas}\left(i,\omega_{seismic}\right)}\left(\frac{\omega_{\ell m}}{\omega_{seismic}}\right)^{-\alpha} \tag{B4}$$

Finally, the term $\Delta\left(Q^{-1}_{\ell mpq}\right)$ was estimated at the beginning of Section 6, with ΔQ^{-1}_{2200} being about 9%.

Therefore, the total error on $Q_{\mu,unc.}\left(r,\omega_{\ell m}\right)$ is dominated by the error of the seismic measurements if $\Delta Q_{\mu,meas}\left(i,\omega_{\ell m}\right)$ is greater than 13%. This is assuming physically realistic values for $Q_{\mu,meas}$ (its value not being too small) and seismic observations being sensitive to deep parts of the mantle (seismic measurements limited to the crust or lithosphere would then barely impact $Q_{\mu,unc.}$).

To illustrate the error propagation and how the determination of seismic attenuation helps distinguishing between our models, we can (as in Section 6.2) assume having a measurement of $Q_{\mu,meas} = 2{,}000 \pm 500$ in the lower mantle of Mars at 1s for $\alpha = 0.33$ can be converted at tidal frequencies as $Q_\mu\left(D, \omega_{T_2}\right) = 76 \pm 19$. From Table 4, the contribution of the lower mantle is on average 35% the total attenuation of the Martian mantle, so $Q_{unc}\left(r, \omega_{T_2}\right)$ from Equation 25 will refer to the remaining 65% of the average bulk $Q_{2200} = 93.0 \pm 8.40$ from Equation 19. This would give us for our averaged model $Q_{unc}\left(r, \omega_{T_2}\right) = 107.2$, which is well defined since $Q_\mu\left(D, \omega_{T_2}\right) = 76 \pm 19$ is close to our model values in Figure 3. From Equation B4, since $Q_{\mu,unc}$ (hence Γ) is well-defined and the relative error on the seismic measurement $\Delta Q_{\mu,meas}$ is 25%, the middle term will dominate the error on our estimate and reach 35% when taking into account the error on the bulk Q_{2200}. Therefore, if we have a measurement of $Q_{\mu,meas} = 2{,}000 \pm 500$ in the lower mantle of Mars at 1s for $\alpha = 0.33$, we can estimate having $Q_\mu\left(D, \omega_{T_2}\right) = 76 \pm 19$ in the lower mantle and $Q_{\mu,unc}\left(r, \omega_{T_2}\right) = 107.2 \pm 37.5$ in the rest of the Martian mantle, translating into $Q_{\mu,unc}(r, \omega_{1s}) = 2{,}820 \pm 987$ at seismic frequencies as given at the end of Section 6.2.

Once again, we note that the actual value of the frequency dependence α directly impact this estimation, while α can also be constrained if the seismic measurements are accurate enough to distinguish the models as shown in Figure 5.

Data Availability Statement

All Martian interior models used in this paper are published in previous papers quoted in Section 4 and Supporting Information S1 for more details on their construction. As indicated there, the FN models are based on Nimmo and Faul (2013), the AB models are based on Khan et al. (2018) and Bagheri et al. (2019), the HS models are based on Samuel et al. (2019, 2021), the TG model is based on Zharkov et al. (2017), and the AR models are based on Rivoldini et al. (2011) and Plesa et al. (2018). No new data were used in this work. The values of physical and orbital parameters of the Martian system used are from previous studies given in Table 1, and results were obtained following the same methods as their original publications.

Acknowledgments
Numerical computations were partly performed on the S-CAPAD platform, IPGP, France. This work is supported in part by the NASA InSight participating scientist program (NNH17ZDA001N-INSTPSP). Tamara Gudkova thanks a government contract of the Schmidt Institute of Physics of the Earth of the Russian Academy of Sciences. Amirhossein Bagheri was supported by a grant from the Swiss National Science Foundation (project 172508). The work of Attilio Rivoldini was financially supported by the Belgian PRODEX program managed by the European Space Agency in collaboration with the Belgian Federal Science Policy Office. Ana-Catalina Plesa acknowledges the financial support and endorsement from the DLR Management Board Young Research Group Leader Program and the Executive Board Member for Space Research and Technology. We thank the reviewers Mathieu Dumberry and Michael Efroimsky for their comments which improved this manuscript. This paper is InSight contribution number 247.

References

Alterman, Z., Jarosch, H., & Pekeris, C. L. (1959). Oscillations of the Earth. *Proceedings of the Royal Society A: Mathematical, Physical and Engineering Sciences*, *252*(1268), 80–95. https://doi.org/10.1098/rspa.1959.0138

Bagheri, A., Khan, A., Al-Attar, D., Crawford, O., & Giardini, D. (2019). Tidal response of Mars constrained from laboratory-based viscoelastic dissipation models and geophysical data. *Journal of Geophysical Research: Planets*, *124*(11), 2703–2727. https://doi.org/10.1029/2019JE006015

Bagheri, A., Khan, A., Efroimsky, M., Kruglyakov, M., & Giardini, D. (2021). Dynamical evidence for Phobos and Deimos as remnants of a disrupted common progenitor. *Nature Astronomy*, *5*(6), 539–543. https://doi.org/10.1038/s41550-021-01306-2

Banerdt, W. B., Smrekar, S., Lognonné, P., Spohn, T., Asmar, S. W., Banfield, D., et al. (2013). InSight: A discovery mission to explore the interior of Mars. In *Paper presented at 44th Annual Lunar and Planetary Science Conference* (Vol. 44, p. 1915).

Banerdt, W. B., Smrekar, S. E., Banfield, D., Giardini, D., Golombek, M., Johnson, C. L., et al. (2020). Initial results from the InSight mission on Mars. *Nature Geoscience*, *13*(3), 183–189. https://doi.org/10.1038/s41561-020-0544-y

Baratoux, D., Toplis, M. J., Monnereau, M., & Gasnault, O. (2011). Thermal history of Mars inferred from orbital geochemistry of volcanic provinces. *Nature*, *472*(7343), 338–341. https://doi.org/10.1038/nature09903

Bills, B. G., Neumann, G. A., Smith, D. E., & Zuber, M. T. (2005). Improved estimate of tidal dissipation within Mars from MOLA observations of the shadow of Phobos. *Journal of Geophysical Research*, *110*(E7), E07004. https://doi.org/10.1029/2004JE002376

Boué, G., & Efroimsky, M. (2019). Tidal evolution of the Keplerian elements. *Celestial Mechanics and Dynamical Astronomy*, *131*(7), 1–46. https://doi.org/10.1007/s10569-019-9908-2

Broquet, A., Wieczorek, M. A., & Fa, W. (2020). Flexure of the lithosphere beneath the north polar cap of Mars: Implications for ice composition and heat flow. *Geophysical Research Letters*, *47*(5), e2019GL086746. https://doi.org/10.1029/2019GL086746

Broquet, A., Wieczorek, M. A., & Fa, W. (2021). The composition of the south polar cap of Mars derived from orbital data. *Journal of Geophysical Research: Planets*, *126*(8), e2020JE006730. https://doi.org/10.1029/2020JE006730

Castillo-Rogez, J. C., & Banerdt, W. B. (2012). Impact of anelasticity on Mars' dissipative properties — Application to the InSight Mission. In *The mantle of Mars: Insights from theory, geophysics, high-pressure studies, and meteorites* (Vol. *1684*, p. 4).

Connolly, J. A. D. (2009). The geodynamic equation of state: What and how. *Geochemistry, Geophysics, Geosystems*, *10*(10), Q10014. https://doi.org/10.1029/2009GC002540

Efroimsky, M., & Lainey, V. (2007). Physics of bodily tides in terrestrial planets and the appropriate scales of dynamical evolution. *Journal of Geophysical Research*, *112*(E12), E12003. https://doi.org/10.1029/2007JE002908

Efroimsky, M., & Makarov, V. V. (2013). Tidal friction and tidal lagging. applicability limitations of a popular formula for the tidal torque. *The Astrophysical Journal*, *764*(1), 26. https://doi.org/10.1088/0004-637x/764/1/26

Efroimsky, M., & Williams, J. G. (2009). Tidal torques: A critical review of some techniques. *Celestial Mechanics and Dynamical Astronomy*, *104*(3), 257–289. https://doi.org/10.1007/s10569-009-9204-7

Folkner, W. M., Dehant, V., Le Maistre, S., Yseboodt, M., Rivoldini, A., Van Hoolst, T., et al. (2018). The rotation and interior structure experiment on the InSight mission to Mars. *Space Science Reviews*, *214*(5), 100. https://doi.org/10.1007/s11214-018-0530-5

Genova, A., Goossens, S., Lemoine, F. G., Mazarico, E., Neumann, G. A., Smith, D. E., & Zuber, M. T. (2016). Seasonal and static gravity field of Mars from MGS, Mars Odyssey and MRO radio science. *Icarus*, *272*, 228–245. https://doi.org/10.1016/j.icarus.2016.02.050

Grott, M., & Breuer, D. (2008). The evolution of the Martian elastic lithosphere and implications for crustal and mantle rheology. *Icarus*, *193*(2), 503–515. https://doi.org/10.1016/j.icarus.2007.08.015

Hartmann, W. K., Malin, M., McEwen, A., Carr, M., Soderblom, L., Thomas, P., et al. (1999). Evidence for recent volcanism on Mars from crater counts. *Nature*, *397*(6720), 586–589. https://doi.org/10.1038/17545

Jackson, I., & Faul, U. H. (2010). Grainsize-sensitive viscoelastic relaxation in olivine: Towards a robust laboratory-based model for seismological application. *Physics of the Earth and Planetary Interiors*, *183*(1–2), 151–163. https://doi.org/10.1016/j.pepi.2010.09.005

Jacobson, R. A. (2010). The orbits and masses of the Martian satellites and the libration of Phobos. *The Astronomical Journal*, *139*(2), 668–679. https://doi.org/10.1088/0004-6256/139/2/668

Jacobson, R. A., & Lainey, V. (2014). Martian satellite orbits and ephemerides. *Planetary and Space Science*, *102*, 35–44. https://doi.org/10.1016/j.pss.2013.06.003

Kaula, W. M. (1964). Tidal dissipation by solid friction and the resulting orbital evolution. *Reviews of Geophysics*, *2*(4), 661–685. https://doi.org/10.1029/RG002i004p00661

Khan, A., & Connolly, J. A. D. (2008). Constraining the composition and thermal state of Mars from inversion of geophysical data. *Journal of Geophysical Research*, *113*(E7), E07003. https://doi.org/10.1029/2007JE002996

Khan, A., Ceylan, S., van Driel, M., Giardini, D., Lognonné, P., Samuel, H., et al. (2021). Upper mantle structure of Mars from InSight seismic data. *Science*, *373*(6553), 434–438. https://doi.org/10.1126/science.abf2966

Khan, A., Liebske, C., Rozel, A., Rivoldini, A., Nimmo, F., Connolly, J. A. D., et al. (2018). A geophysical perspective on the bulk composition of Mars. *Journal of Geophysical Research: Planets*, *123*(2), 575–611. https://doi.org/10.1002/2017JE005371

Khan, A., Sossi, P., Liebske, C., Rivoldini, A., & Giardini, D. (2022). Geophysical and cosmochemical evidence for a volatile-rich Mars. *Earth and Planetary Science Letters*, *578*, 117330. https://doi.org/10.1016/j.epsl.2021.117330

Konopliv, A. S., Asmar, S. W., Folkner, W. M., Karatekin, O., Nunes, D. C., Smrekar, S. E., et al. (2011). Mars high resolution gravity fields from MRO, Mars seasonal gravity, and other dynamical parameters. *Icarus*, *211*(1), 401–428. https://doi.org/10.1016/j.icarus.2010.10.004

Konopliv, A. S., Park, R. S., & Folkner, W. M. (2016). An improved JPL Mars gravity field and orientation from Mars orbiter and lander tracking data. *Icarus*, *274*, 253–260. https://doi.org/10.1016/j.icarus.2016.02.052

Konopliv, A. S., Park, R. S., Rivoldini, A., Baland, R.-M., Le Maistre, S., Van Hoolst, T., et al. (2020). Detection of the Chandler wobble of Mars from orbiting spacecraft. *Geophysical Research Letters*, *47*(21), e2020GL090568. https://doi.org/10.1029/2020GL090568

Lainey, V., Dehant, V., & Pätzold, M. (2007). First numerical ephemerides of the Martian moons. *Astronomy & Astrophysics*, *465*(3), 1075–1084. https://doi.org/10.1051/0004-6361:20065466

Lognonné, P., Banerdt, W. B., Giardini, D., Pike, W. T., Christensen, U., Laudet, P., et al. (2019). SEIS: Insight's seismic experiment for internal structure of Mars. *Space Science Reviews*, *215*, 12. https://doi.org/10.1007/s11214-018-0574-6

Lognonné, P., Banerdt, W. B., Pike, W. T., Giardini, D., Christensen, U., Garcia, R. F., et al. (2020). Constraints on the shallow elastic and anelastic structure of Mars from InSight seismic data. *Nature Geoscience*, *13*(3), 213–220. https://doi.org/10.1038/s41561-020-0536-y

Lognonné, P., & Mosser, B. (1993). Planetary seismology. *Surveys in Geophysics*, *14*(3), 239–302. https://doi.org/10.1007/BF00690946

Love, A. E. H. (1911). *Some problems of geodynamics* (Vol. 1). Cambridge University Press.

MacDonald, G. J. F. (1964). Earth and Moon: Past and future. *Science*, *145*(3635), 881–890. https://doi.org/10.1126/science.145.3635.881

Murray, C. D., & Dermott, S. F. (2000). *Solar system dynamics*. Cambridge University Press.

Neukum, G., Jaumann, R., Hoffmann, H., Hauber, E., Head, J. W., Basilevsky, A. T., et al. (2004). Recent and episodic volcanic and glacial activity on Mars revealed by the High Resolution Stereo Camera. *Nature*, *432*(7020), 971–979. https://doi.org/10.1038/nature03231

Nimmo, F., & Faul, U. H. (2013). Dissipation at tidal and seismic frequencies in a melt-free, anhydrous Mars. *Journal of Geophysical Research: Planets*, *118*(12), 2558–2569. https://doi.org/10.1002/2013JE004499

Padovan, S., Margot, J.-L., Hauck, S. A., Moore, W. B., & Solomon, S. C. (2014). The tides of Mercury and possible implications for its interior structure. *Journal of Geophysical Research: Planets*, *119*(4), 850–866. https://doi.org/10.1002/2013JE004459

Plesa, A.-C., Grott, M., Tosi, N., Breuer, D., Spohn, T., & Wieczorek, M. A. (2016). How large are present-day heat flux variations across the surface of Mars? *Journal of Geophysical Research: Planets*, *121*(12), 2386–2403. https://doi.org/10.1002/2016JE005126

Plesa, A.-C., Padovan, S., Tosi, N., Breuer, D., Grott, M., Wieczorek, M. A., et al. (2018). The thermal state and interior structure of Mars. *Geophysical Research Letters*, *45*(22), 12198–12209. https://doi.org/10.1029/2018GL080728

Pätzold, M., Andert, T. P., Tyler, G. L., Asmar, S. W., Häusler, B., & Tellmann, S. (2014). Phobos mass determination from the very close flyby of Mars Express in 2010. *Icarus*, *229*, 92–98. https://doi.org/10.1016/j.icarus.2013.10.021

Redmond, J. C., & Fish, F. F. (1964). The luni-tidal interval in Mars and the secular acceleration of Phobos. *Icarus*, *3*(2), 87–91. https://doi.org/10.1016/0019-1035(64)90048-X

Renaud, J. P., Henning, W. G., Saxena, P., Neveu, M., Bagheri, A., Mandell, A., & Hurford, T. (2021). Tidal dissipation in dual-body, highly eccentric, and nonsynchronously rotating systems: Applications to Pluto–Charon and the exoplanet TRAPPIST-1e. *The Planetary Science Journal*, *2*(1), 4. https://doi.org/10.3847/psj/abc0f3

Rivoldini, A., Van Hoolst, T., Verhoeven, O., Mocquet, A., & Dehant, V. (2011). Geodesy constraints on the interior structure and composition of Mars. *Icarus*, *213*(2), 451–472. https://doi.org/10.1016/j.icarus.2011.03.024

Samuel, H., Ballmer, M. D., Padovan, S., Tosi, N., Rivoldini, A., & Plesa, A.-C. (2021). The thermo-chemical evolution of Mars with a strongly stratified mantle. *Journal of Geophysical Research: Planets*, *126*(4), 1–61. https://doi.org/10.1029/2020je006613

Samuel, H., Lognonné, P., Panning, M., & Lainey, V. (2019). The rheology and thermal history of Mars revealed by the orbital evolution of Phobos. *Nature*, *569*(7757), 523–527. https://doi.org/10.1038/s41586-019-1202-7

Seidelmann, P. K., Archinal, B. A., A'hearn, M. F., Conrad, A., Consolmagno, G. J., Hestroffer, D., et al. (2007). Report of the IAU/IAG Working Group on cartographic coordinates and rotational elements: 2006. *Celestial Mechanics and Dynamical Astronomy*, *98*(3), 155–180. https://doi.org/10.1007/s10569-007-9072-y

Shida, T. (1912). On the body tides of the Earth, a proposal for the International Geodetic Association. *Proceedings of the Tokyo Mathematico-Physical Society. 2nd Series*, *6*(16), 242–258. https://doi.org/10.11429/ptmps1907.6.16_242

Smrekar, S. E., Lognonné, P., Spohn, T., Banerdt, W. B., Breuer, D., Christensen, U., et al. (2018). Pre-mission InSights on the interior of Mars. *Space Science Reviews*, *215*(1), 3. https://doi.org/10.1007/s11214-018-0563-9

Stixrude, L., & Lithgow-Bertelloni, C. (2005). Thermodynamics of mantle minerals — I. Physical properties. *Geophysical Journal International*, *162*(2), 610–632. https://doi.org/10.1111/j.1365-246X.2005.02642.x

Stixrude, L., & Lithgow-Bertelloni, C. (2011). Thermodynamics of mantle minerals - II. Phase equilibria. *Geophysical Journal International*, *184*(3), 1180–1213. https://doi.org/10.1111/j.1365-246X.2010.04890.x

Stähler, S. C., Khan, A., Banerdt, W. B., Lognonné, P., Giardini, D., Ceylan, S., et al. (2021). Seismic detection of the Martian core. *Science*, *373*(6553), 443–448. https://doi.org/10.1126/science.abi7730

Takeuchi, H., & Saito, M. (1972). Seismic surface waves. In B. A. Bolt (Ed.), *Methods in Computational Physics: Advances in Research and Applications* (Vol. 11, pp. 217–295). Elsevier. https://doi.org/10.1016/B978-0-12-460811-5.50010-6

Taylor, G. J. (2013). The bulk composition of Mars. *Chemie der Erde - Geochemistry*, *73*(4), 401–420. https://doi.org/10.1016/j.chemer.2013.09.006

Taylor, P. A., & Margot, J.-L. (2010). Tidal evolution of close binary asteroid systems. *Celestial Mechanics and Dynamical Astronomy*, *108*(4), 315–338. https://doi.org/10.1007/s10569-010-9308-0

Tobie, G., Grasset, O., Lunine, J. I., Mocquet, A., & Sotin, C. (2005). Titan's internal structure inferred from a coupled thermal-orbital model. *Icarus*, *175*(2), 496–502. https://doi.org/10.1016/j.icarus.2004.12.007

Van Hoolst, T., Dehant, V., Roosbeek, F., & Lognonné, P. (2003). Tidally induced surface displacements, external potential variations, and gravity variations on Mars. *Icarus*, *161*(2), 281–296. https://doi.org/10.1016/S0019-1035(02)00045-3

Verhoeven, O., Rivoldini, A., Vacher, P., Mocquet, A., Choblet, G., Menvielle, M., et al. (2005). Interior structure of terrestrial planets: Modeling Mars' mantle and its electromagnetic, geodetic, and seismic properties. *Journal of Geophysical Research*, *110*(E4), E04009. https://doi.org/10.1029/2004JE002271

Wänke, H., & Dreibus, G. (1994). Chemistry and accretion history of Mars. *Philosophical Transactions: Physical Sciences and Engineering*, *349*(1), 285–293.

Wieczorek, M. A., & Zuber, M. T. (2004). Thickness of the Martian crust: Improved constraints from geoid-to-topography ratios. *Journal of Geophysical Research*, *109*(E1), E01009. https://doi.org/10.1029/2003JE002153

Yoder, C. F., Konopliv, A. S., Yuan, D. N., Standish, E. M., & Folkner, W. M. (2003). Fluid core size of Mars from detection of the solar tide. *Science*, *300*(5617), 299–303. https://doi.org/10.1126/science.1079645

Yoshizaki, T., & McDonough, W. F. (2020). The composition of Mars. *Geochimica et Cosmochimica Acta*, *273*, 137–162. https://doi.org/10.1016/j.gca.2020.01.011

Zharkov, V. N., & Gudkova, T. V. (1997). On the dissipative factor of the Martian interiors. *Planetary and Space Science*, *45*(4), 401–407. https://doi.org/10.1016/S0032-0633(96)00144-4

Zharkov, V. N., & Gudkova, T. V. (2005). Construction of Martian interior model. *Solar System Research*, *39*(5), 343–373. https://doi.org/10.1007/s11208-005-0049-7

Zharkov, V. N., Gudkova, T. V., & Batov, A. V. (2017). On estimating the dissipative factor of the Martian interior. *Solar System Research*, *51*(6), 479–490. https://doi.org/10.1134/S0038094617060089

Zharkov, V. N., Gudkova, T. V., & Molodensky, S. M. (2009). On models of Mars' interior and amplitudes of forced nutations: 1. The effects of deviation of Mars from its equilibrium state on the flattening of the core–mantle boundary. *Physics of the Earth and Planetary Interiors*, *172*(3), 324–334. https://doi.org/10.1016/j.pepi.2008.10.009

References From the Supporting Information

Babeyko, A., & Zharkov, V. (2000). Martian crust: A modeling approach. *Physics of the Earth and Planetary Interiors*, *117*(1), 421–435. https://doi.org/10.1016/S0031-9201(99)00111-9

Bertka, C. M., & Fei, Y. (1997). Mineralogy of the Martian interior up to core-mantle boundary pressures. *Journal of Geophysical Research*, *102*(B3), 5251–5264. https://doi.org/10.1029/96JB03270

Bertka, C. M., & Fei, Y. (1998). Density profile of an SNC model Martian interior and the moment-of-inertia factor of Mars. *Earth and Planetary Science Letters*, *157*(1), 79–88. https://doi.org/10.1016/S0012-821X(98)00030-2

Boynton, W. V., Taylor, G. J., Evans, L. G., Reedy, R. C., Starr, R., Janes, D. M., et al. (2007). Concentration of H, Si, Cl, K, Fe, and Th in the low- and mid-latitude regions of Mars. *Journal of Geophysical Research*, *112*(12), 1–15. https://doi.org/10.1029/2007JE002887

Greeley, R., & Schneid, B. D. (1991). Magma generation on Mars: Amounts, rates, and comparisons with Earth, Moon, and Venus. *Science*, *254*(5034), 996–998. https://doi.org/10.1126/science.254.5034.996

Khan, A., Mosegaard, K., Williams, J. G., & Lognonné, P. (2004). Does the Moon possess a molten core? Probing the deep lunar interior using results from LLR and Lunar Prospector. *Journal of Geophysical Research*, *109*(E9), 80. https://doi.org/10.1029/2004je002294

Knapmeyer-Endrun, B., Panning, M. P., Bissig, F., Joshi, R., Khan, A., Kim, D., et al. (2021). Thickness and structure of the Martian crust from InSight seismic data. *Science*, *373*(6553), 438–443. https://doi.org/10.1126/science.abf8966

Morschhauser, A., Grott, M., & Breuer, D. (2011). Crustal recycling, mantle dehydration, and the thermal evolution of Mars. *Icarus*, *212*(2), 541–558. https://doi.org/10.1016/j.icarus.2010.12.028

Nimmo, F., & Tanaka, K. (2005). Early crustal evolution of Mars. *Annual Review of Earth and Planetary Sciences*, *33*(1), 133–161. https://doi.org/10.1146/annurev.earth.33.092203.122637

Ohtani, E., Suzuki, A., & Kato, T. (1998). Flotation of olivine and diamond in mantle melt at high pressure: Implications for fractionation in the deep mantle and ultradeep origin of diamond. In *Properties of Earth and planetary materials at high pressure and temperature* (pp. 227–239). American Geophysical Union (AGU).

Terasaki, H., Rivoldini, A., Shimoyama, Y., Nishida, K., Urakawa, S., Maki, M., et al. (2019). Pressure and composition effects on sound velocity and density of core-forming liquids: Implication to core compositions of terrestrial planets. *Journal of Geophysical Research: Planets*, *124*(8), 2272–2293. https://doi.org/10.1029/2019JE005936